Computer Assisted Methods in Engineering and Science, **22**: 3–30, 2015.

Application and analysis of an adaptive wave-based technique based on a boundary error indicator for the sound radiation simulation of a combustion engine model

Tamás Mócsai[1], Franz Diwoky[2], Achim Hepberger[2], Hans-Herwig Priebsch[3], Fulop Augusztinovicz[1]

[1] *Budapest University of Technology and Economics*
Laboratory of Vibroacoustics
Department of Telecommunications
H-1117, Magyar Tudosok korutja 3., Budapest, Hungary
e-mail: mocsai@hit.bme.hu

[2] *AVL List GmbH*
Hans-List Platz 1, A-8020, Graz, Austria

[3] *Virtual Vehicle Competence Center*
Inffeldgasse 21, A-8010, Graz, Austria

In recent years, Trefftz methods have received increasing attention, as being alternatives of the already well-established element-based simulation methods (e.g., finite element and boundary element methods). The wave-based technique is based on the indirect Trefftz approach for the solution of steady-state, time-harmonic acoustic problems.

The dynamic field variables are expanded in terms of wave functions, which satisfy the governing partial differential equation, but do not necessarily satisfy the imposed boundary conditions. Therefore, the approximation error of the method is exclusively caused by the error on the boundary, since there is no additional error present in the domain. The authors investigate the potentials of a novel boundary error indicator-controlled adaptive local refinement strategy. Practical, industrial-oriented application of the method is presented on the 3D free-field sound radiation model of a simplified combustion engine. Results and efficiency of the approach are compared to *a priori*, frequency-dependent global refinement strategies.

Keywords: Trefftz method, adaptivity, error indicator, boundary error, Wave Based Technique, engine sound, numerical acoustics.

1. Introduction

The finite element method (FEM) [1, 2] and the boundary element method (BEM) [3, 4] has become common tools to evaluate vibroacoustic characteristics of virtual prototypes. However, calculation time is still a critical issue in most simulation cases, which limits their applicability to the low-frequency region. Standard FE and BE techniques perform satisfactorily in the low-frequency range, where k^2h is sufficiently small (k is the physical wave number, h is the element size) and the error of standard FE and BE formulations is governed by the interpolation error [5, 6], which is practically achieved using 6–10 elements per wavelength. Typically, FE numerical solutions get polluted at higher frequencies, and the error becomes governed by the numerical dispersion. While the pollution error is less pronounced in BE solutions [7, 8], global mesh refinement for both methods leads to excessive calculation times, if the frequency range of interest is extended towards

high frequencies. Moreover, in a typical industrial FE or BE simulation process, one single mesh is used to cover the full frequency range of interest. As the mesh discretization is determined by the highest frequency of interest, the model is typically over-discretized for the lower frequency ranges.

The error of numerical solutions has always been an important research topic, as information on these errors can provide a way to assess the reliability of the computation, and a basis for adaptive control of the calculation. Estimates or information on the error is usually given in two different manners. *A priori* error estimates are obtained before the solution is known, and they are useful for the analysis of numerical methods, e.g., to determine the rate of convergence and its dependence on problem parameters. They are usually not computable, because they are expressed in terms of the unknown exact solution. Babuska [9] and Ihlenburg [6] derived *a priori* estimates for the finite element solution of the Helmholtz equation, in which they took into account the pollution error too. Ihlenburg [10] provided practical frequency limits, and mesh resolution requirements based on the above *a priori* estimates, considering the excessive growth of the pollution error, when k^2h is not small.

A posteriori error estimates are calculated by post-processing the numerical solution, and they are typically residual (implicit or explicit), or recovery type. Oden [11] provides a good survey of existing techniques for error estimation in FEM; an overview on the topic specifically for Hemholtz problems is also given [12]. Most notably, Stewart and Hughes [13–15] derived an explicit residual-based error estimator for the exterior Helmholtz problem, along with an *hp*-adaptive strategy, and a computable scaling constant to provide an exact error bound. Bouillard [16] gave standard explicit residual estimates, while Babuska [17–19] studied implicit residual error estimates. Bouillard and Ihlenburg provided a gradient recovery-based error estimator [20], and attempts to provide *a posteriori* estimates taking into account the pollution error were reported by Babuska [21]. Goal-oriented estimates represent a new class of *a posteriori* estimates [22, 23] and they provide the basis for goal-oriented adaptive methods. For BEM, *a priori* estimates have recently been studied [7, 24]. The BEM methods suffer from the pollution effect far less then FEM [7, 8]. *A posteriori* error estimators and adaptive strategies for BEM have been studied, e.g., in [25, 26] and a good overview on the topic can be found in a survey from Kita [27].

The goal of adaptivity is generally computational efficiency, namely to achieve a given solution accuracy at a reduced problem size or to provide a more accurate solution given at a fixed problem size. An adaptive calculation consists of two parts: the *a posteriori* error estimator/indicator and the adaptive strategy. The latter transforms the information on the error into specifications for an improved calculation. The enhanced computational efficiency of adaptive methods is achieved by local refinement, (rather than global refinement), which increases the number of DOFs in regions where the solution errors are high. In case of FEM, the process of h-refinement involves specification of new element sizes, holding the polynomial order of the finite element shape functions, p, fixed. In the case of p-refinement, the element size h is held fixed while p is specified locally. Finally, hp-refinement involves local specification of both.

In addition to recent advances in the field of element-based methods (e.g., for FEM [28–30], and BEM [31–33]), research and application of alternative approaches, e.g., the so-called Trefftz [34] methods have also gained increasing interest. Similarly to BEM, indirect and direct formulations [35] of the Trefftz approach are distinguished. For time-harmonic acoustics, the indirect Trefftz approach is preferred, enumerating several implementations. The shape functions in the indirect Trefftz approach satisfy the governing differential equation, but do not necessarily satisfy the boundary conditions. Therefore, the approximation error of the method is exclusively caused by the error on the boundary, since there is no additional error present in the domain. For a more detailed overview on Trefftz methods for Helmholtz problems see, e.g., [36, 37].

This paper concentrates on the application of one particular Trefftz method, the wave-based technique [38], which is an indirect, frameless (or meshless) Trefftz method. The wave-based technique has been successfully tested in both academic and industrial-sized validation cases in structural [39, 40], acoustic [41–43] and coupled vibroacoustic problems [44–48]. The aim of this paper

is to present the application and analysis of a novel adaptive calculation strategy-based on *a posteriori* boundary error indicators to the industrial simulation of sound radiation from a combustion engine. Efficiency of the adaptive scheme is compared to *a priori*, frequency-dependent, global refinement strategies. The validation is carried out on a simplified, yet industrial-sized 3D example up to the mid-frequency range (the Helmholtz number being $H_e = kL \approx 42$ for the present engine model at the highest calculation frequency). The presented industrial-oriented example extends others' [42, 43] and the authors' [49–53] recent work on WBT for 3D exterior acoustics applications.

The outline of the paper is the following: Sec. 2 presents the general problem definition for exterior time-harmonic acoustics, and summarizes the wave-based modeling methodology and solution scheme for such problems. Section 3 deals with the definition of the proposed *a posteriori* error indicator and the adaptive control strategy of the wave function set. Section introduces an industrial-like model of a passenger car engine and provides an overview of the applied engine model, and the used engine simulation tool. Section 6 gives analysis and discussion of the numerical models and their results in detail. Finally, Sec. 7 summarizes the findings of this paper with general remarks on the presented strategy.

2. The concept of wave-based technique for exterior Helmholtz problems

Let us consider the exterior acoustic problem depicted in Fig. 1. The boundary Γ is surrounded by the fluid domain Ω. The fluid is characterized by the speed of sound c and the ambient fluid density ρ_0. The time-harmonic pressure response is given by $p(\mathbf{r}, t) = p(\mathbf{r})\mathrm{e}^{j\omega t}$ at position $\mathbf{r}$, where j represents the imaginary unit, t the time and ω the circular frequency. Under the assumption

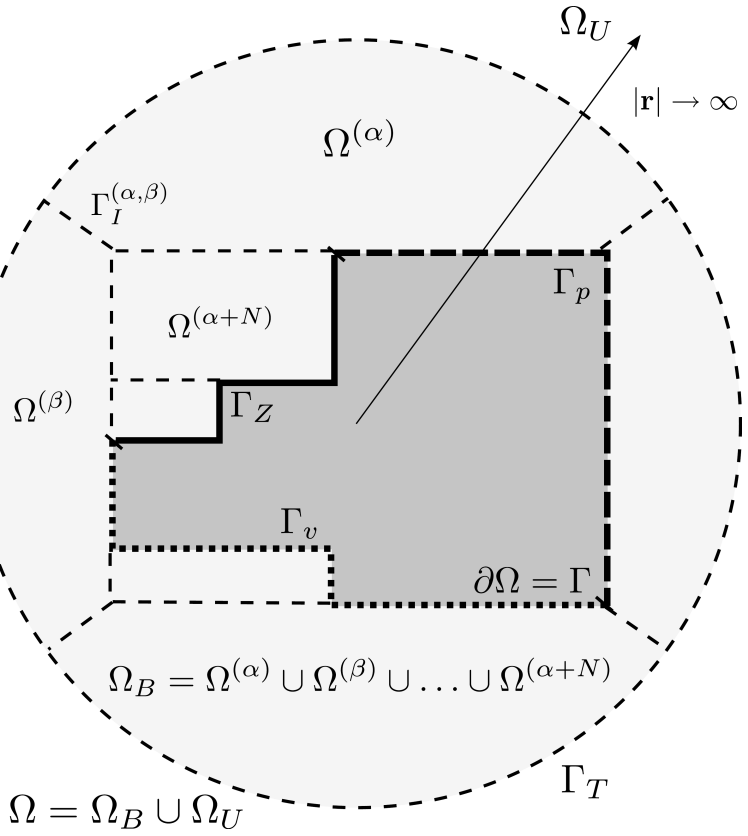

Fig. 1. A general exterior Helmholtz problem definition.

that the system is linear, the fluid is inviscid and the process is adiabatic, the steady-state pressure field is governed by the homogenous Helmholtz equation, if no other sources are present, i.e.,

$$\nabla^2 p(\mathbf{r}) + k^2 p(\mathbf{r}) = 0, \tag{1}$$

where ∇^2 is the Laplace operator, $k = \omega/c$ is the physical wave number. The physical boundary consists of three non-overlapping parts, $\Gamma = \Gamma_p \cup \Gamma_v \cup \Gamma_Z$, where the corresponding boundary conditions are imposed: pressure (Dirichlet) boundary condition $\overline{p}(\mathbf{r})$ on Γ_p, the normal velocity (Neumann) boundary condition $\overline{v}_n(\mathbf{r})$ on Γ_v and the normal impedance (Robin) boundary condition $\overline{Z}_n(\mathbf{r})$ on Γ_Z. In addition to the above mentioned conditions, the solution $p(\mathbf{r})$ of an unbounded problem has to satisfy the Sommerfeld-radiation condition.

$$\lim_{|\mathbf{r}|\to\infty} \left[|\mathbf{r}| \left(\frac{\partial p(\mathbf{r})}{\partial |\mathbf{r}|} + jkp(\mathbf{r}) \right) \right] = 0. \tag{2}$$

The physical meaning of this condition is that there are no sources of energy at infinity and as such, the exterior solution vanishes at infinity. The Helmholtz equation, together with the associated boundary conditions, defines a unique pressure field $p(\mathbf{r})$.

2.1. Partitioning into subdomains

For the method to converge, the underlying bounded acoustic domain has to be partitioned into a number of large convex or non-convex, but geometrically restricted subdomains [54]. Within each of those subdomains, the field variables are expressed as an expansion of wave functions that intrinsically satisfy the governing Helmholtz equation. The degrees of freedom are the coefficients of the wave functions in this expansion. In order to tackle problems in unbounded domains, the problem domain is divided into a bounded region Ω_B and an unbounded region Ω_U by introducing an artificial truncation boundary Γ_T. The total number of subdomains, including the unbounded domain Ω_U is denoted by N_Ω, the number of subdomains only within Ω_B is denoted by N_{Ω^B}. Figure 1 depicts the subdivision of domain Ω to the bounded part Ω_B and unbounded part Ω_U, and the subdivision of Ω_B to bounded subdomains. Domains $\Omega^{(\alpha)}$ and $\Omega^{(\beta)}$ represent two subdomains, which are adjacent, having a common coupling interface $\Gamma_I^{(\alpha,\beta)} \neq \emptyset$. Domain $\Omega^{(\alpha+N)}$ depicts the last bounded subdomain, whose index is $\alpha + N = N_{\Omega^B}$.

The boundary of a bounded subdomain $\Omega^{(\alpha)}$ consists of the following non-overlapping parts: $\partial\Omega^{(\alpha)} = \Gamma_p^{(\alpha)} \cup \Gamma_v^{(\alpha)} \cup \Gamma_Z^{(\alpha)} \cup \Gamma_I^{(\alpha)}$, where $\Gamma_p^{(\alpha)} = \Gamma_p \cap \partial\Omega^{(\alpha)}$, $\Gamma_v^{(\alpha)} = \Gamma_v \cap \partial\Omega^{(\alpha)}$, $\Gamma_Z^{(\alpha)} = \Gamma_Z \cap \partial\Omega^{(\alpha)}$, and $\Gamma_I^{(\alpha)}$ denotes the artificial interfaces to the neighboring subdomains $\Gamma_I^{(\alpha)} = \bigcup_{\beta=1..N_\Omega, \alpha\neq\beta, \partial\Omega^{(\alpha)}\cap\partial\Omega^{(\beta)}\neq\emptyset} \Gamma^{(\alpha,\beta)}$ and to the unbounded domain.

2.2. Wave function selection in the bounded part Ω_B

Within a subdomain $\Omega^{(\alpha)}$ of the bounded part Ω_B of an exterior problem, the steady-state dynamic acoustic pressure field $p^{(\alpha)}(\mathbf{r})$ is approximated using the pressure expansion:

$$p^{(\alpha)}(\mathbf{r}) \approx \widehat{p}^{(\alpha)}(\mathbf{r}) = \sum_{w=1}^{n_w^{(\alpha)}} p_w^{(\alpha)} \phi_w^{(\alpha)}(\mathbf{r}) \qquad \mathbf{r} \in \Omega^{(\alpha)}, \tag{3}$$

where the following T-complete set is used, consisting of the so-called r-, s- and t-sets [38, 55]:

$$\begin{aligned}
\phi_{w_r}^{(\alpha)}(x,y,z) &= \cos\left(k_{x_{wr}}^{(\alpha)} x\right) \cos\left(k_{y_{wr}}^{(\alpha)} y\right) \mathrm{e}^{-jk_{z_{wr}}^{(\alpha)} z}, \\
\phi_{w_s}^{(\alpha)}(x,y,z) &= \cos\left(k_{x_{ws}}^{(\alpha)} x\right) \mathrm{e}^{-jk_{y_{ws}}^{(\alpha)} y} \cos\left(k_{z_{ws}}^{(\alpha)} z\right), \\
\phi_{w_t}^{(\alpha)}(x,y,z) &= \mathrm{e}^{-jk_{x_{wt}}^{(\alpha)} x} \cos\left(k_{y_{wt}}^{(\alpha)} y\right) \cos\left(k_{z_{wt}}^{(\alpha)} z\right),
\end{aligned} \tag{4}$$

where $n_{w_r}^{(\alpha)} + n_{w_s}^{(\alpha)} + n_{w_t}^{(\alpha)} = n_w^{(\alpha)}$, and the parameters $k_{x_{w\bullet}}^{(\alpha)}, k_{y_{w\bullet}}^{(\alpha)}, k_{z_{w\bullet}}^{(\alpha)}$; $\bullet = r, s, t$ (the wave numbers of the corresponding wave-sets) are defined in such a way that the resultant wave set satisfies the homogeneous Helmholtz equation, for which the following setting is used [38]:

$$k_{(x,y,z)_{wr}}^{(\alpha)} = \left(\frac{n_{x_r}^{(\alpha)}\pi}{L_x^{(\alpha)}}, \frac{n_{y_r}^{(\alpha)}\pi}{L_y^{(\alpha)}}, \pm\sqrt{k^2 - (k_{x_{wr}}^{(\alpha)})^2 - (k_{y_{wr}}^{(\alpha)})^2} \right), \tag{5}_1$$

$$k_{(x,y,z)_{ws}}^{(\alpha)} = \left(\frac{n_{x_s}^{(\alpha)}\pi}{L_x^{(\alpha)}}, \pm\sqrt{k^2 - (k_{x_{ws}}^{(\alpha)})^2 - (k_{z_{ws}}^{(\alpha)})^2}, \frac{n_{z_s}^{(\alpha)}\pi}{L_z^{(\alpha)}} \right), \tag{5}_2$$

$$k_{(x,y,z)_{wt}}^{(\alpha)} = \left(\pm\sqrt{k^2 - (k_{y_{wt}}^{(\alpha)})^2 - (k_{z_{wt}}^{(\alpha)})^2}, \frac{n_{y_t}^{(\alpha)}\pi}{L_y^{(\alpha)}}, \frac{n_{z_t}^{(\alpha)}\pi}{L_z^{(\alpha)}} \right), \tag{5}_3$$

where $L_x^{(\alpha)} \dots L_z^{(\alpha)}$ are the dimensions of a rectangular box enclosing the corresponding domain $\Omega^{(\alpha)}$ and $k^2 = (w/c)^2$ is the square of the real wave number. The values $n_{x_\bullet}^{(\alpha)} = 0, 1, \dots N_x^{(\alpha)}$, $n_{y_\bullet}^{(\alpha)} = 0, 1, \dots N_y^{(\alpha)}$ and $n_{z_\bullet}^{(\alpha)} = 0, 1, \dots N_x^{(\alpha)}$ comprise uninterrupted sets of integers, whose maximal values $N_x^{(\alpha)}$,$N_y^{(\alpha)}$ and $N_z^{(\alpha)}$ determine the number of degrees of freedom of the truncated, finite-sized computational model.

2.3. Wave function selection in the unbounded part Ω_U

The solution of an exterior Helmholtz problem has to satisfy the Helmholtz equation (1) and the Sommerfeld-condition (2) in the unbounded domain Ω_U. A valid basis set (referred to as radiation functions) for the wave function expansion in Ω_U is given in spherical coordinates [56]:

$$p^{(\Omega_U)}(r, \phi, \theta) = \sum_{l=0}^{N_{RF}} \sum_{m=-l}^{l} p_{lm} h_l(kr) Y_{lm}(\phi, \theta), \tag{6}$$

where r, ϕ, θ denote the radial, inclination and zenith co-ordinates, respectively, $Y_{lm}(\phi, \theta)$ denotes the spherical harmonics, and $h_l(kr)$ stands for spherical Hankel functions. The radius of the truncation sphere Γ_T plays an important role in determining the numerical size of an exterior wave-based model. A larger truncation radius requires a higher number of wave functions in both Ω_B and Ω_U. Generally, the bigger the truncation radius is, the more radiation functions are needed to describe the exterior pressure field. Bigger truncation radius yields larger subdomains in Ω_B too, in order to fill the enlarged volume. As a consequence, a larger truncation radius requires a higher number of wave functions in Ω_B as well. This influence will be shown on the convergence plots of Subsec. 6.2.1.

2.4. Enforcement of the boundary and interface conditions and solution

In order to represent the boundary value problem in the indirect Trefftz scheme, the boundary and interface conditions are transformed into a weighted residual formulation. The residual error functions corresponding to the physical boundary conditions are defined as

$$R_p^{(\alpha)}(\mathbf{r}) = \widehat{p}^{(\alpha)}(\mathbf{r}) - \overline{p}(\mathbf{r}) \qquad \mathbf{r} \in \Gamma_p^{(\alpha)}, \tag{7}_1$$

$$R_v^{(\alpha)}(\mathbf{r}) = \frac{j}{\rho_o \omega} \frac{\partial}{\partial n} \widehat{p}^{(\alpha)}(\mathbf{r}) - \overline{v}_n(\mathbf{r}) \qquad \mathbf{r} \in \Gamma_v^{(\alpha)}, \tag{7}_2$$

$$R_z^{(\alpha)}(\mathbf{r}) = \frac{j}{\rho_o \omega} \frac{\partial}{\partial n} \widehat{p}^{(\alpha)}(\mathbf{r}) - \frac{\widehat{p}^{(\alpha)}(\mathbf{r})}{\overline{Z}_n(\mathbf{r})} \qquad \mathbf{r} \in \Gamma_z^{(\alpha)}, \tag{7}_3$$

where $\widehat{p}^{(\alpha)}(\mathbf{r})$ denotes the pressure approximation in $\Omega^{(\alpha)}$, obtained by the expansion (3) and $\overline{p}(\mathbf{r})$, $\overline{v}_n(\mathbf{r})$ and $\overline{Z}_n(\mathbf{r})$ denote the prescribed boundary conditions as defined in Sec. 2. Besides the physical boundary conditions, continuity conditions must be applied to the coupling interfaces $\Gamma^{(\alpha,\beta)}$ to ensure continuity between acoustic subdomains $\Omega^{(\alpha)}$ and $\Omega^{(\beta)}$. An impedance coupling approach [55], proposed for WBT, expresses the continuity condition as a linear combination of a direct pressure and velocity continuity condition:

$$Z_c\,\widehat{p}^{(\alpha)}(\mathbf{r}) = Z_c\,\widehat{p}^{(\beta)}(\mathbf{r}),$$

$$\widehat{v}_n^{(\alpha)}(\mathbf{r}) = -\widehat{v}_n^{(\beta)}(\mathbf{r}),$$

which, in a shorthand notation results in the following residual expression:

$$R_I^{(\beta,\alpha)}(\mathbf{r}) = \widehat{v}_n^{(\alpha)} + \widehat{v}_n^{(\beta)} + \frac{1}{Z_c}\left[\widehat{p}^{(\alpha)}(\mathbf{r}) - \widehat{p}^{(\beta)}(\mathbf{r})\right], \tag{8}$$

where $\mathbf{r} \in \Omega_{I_{(\alpha,\beta)}}$, moreover $\widehat{v}_n^{(\alpha)}(\mathbf{r}) = \frac{j}{\rho_o\omega}\frac{\partial}{\partial n}\widehat{p}^{(\alpha)}(\mathbf{r})$ and $\widehat{v}_n^{(\beta)}(\mathbf{r}) = \frac{j}{\rho_o\omega}\frac{\partial}{\partial n}\widehat{p}^{(\beta)}(\mathbf{r})$ are taken using the outward local normal vectors on $\partial\Omega^{(\alpha)}$ and $\partial\Omega^{(\beta)}$ respectively. The impedance coupling factor Z_c is a weighting factor between the pressure and normal velocity field on $\Gamma_{I^{(\alpha,\beta)}}$. The expression (8) represents the continuity error of the pressure and normal velocity fields transformed into the continuity error of an equivalent acoustic velocity quantity. The transformation via the factor Z_c introduces an artificial damping (impedance condition) on $\Gamma_{I^{(\alpha,\beta)}}$, which stabilizes the solution in both $\Omega^{(\alpha)}$ and $\Omega^{(\beta)}$. For exterior problems, the continuity between Ω_U and Ω_B are enforced using (8) as well.

For each subdomain, the residual errors are orthogonalised with respect to a weighting function $\widetilde{p}^{(\alpha)}$ or its derivative:

$$\int_{\Gamma_v^{(\alpha)}} \widetilde{p}^{(\alpha)}(\mathbf{r})R_v(\mathbf{r})\mathrm{d}\Gamma + \int_{\Gamma_Z^{(\alpha)}} \widetilde{p}^{(\alpha)}(\mathbf{r})R_Z(\mathbf{r})\mathrm{d}\Gamma + \int_{\Gamma_p^{(\alpha)}} \frac{j\omega}{\rho_0 c}\frac{\partial}{\partial n}\widetilde{p}^{(\alpha)}(\mathbf{r})R_p(\mathbf{r})\mathrm{d}\Gamma + \sum_{\beta=1,\alpha\neq\beta}^{N_\Omega} \int_{\Gamma_I^{(\alpha,\beta)}} \widetilde{p}^{(\alpha)}(\mathbf{r})R_I^{(\alpha,\beta)}\mathrm{d}\Gamma = 0. \tag{9}$$

The WBT, as well as FEM, applies a Galerkin weighting to orthogonalize the residuals, which uses the basis functions themselves as test (also known as weighting) functions. In case of WBT, the test (or weighting) functions $\widetilde{p}^{(\alpha)}$ are expanded in terms of the same set of acoustic wave functions as in the pressure expansion. This leads to a system of linear equations. The first three terms of (9) (first row) comprise matrix blocks related to the physical boundary conditions, while the last term of (9) (second row) comprises the coupling matrix block pairs related to the continuity conditions (see, e.g., [38, 55] for the definition of the equation structure). The system matrix is a dense, non-symmetric, complex-valued and frequency-dependent matrix. Although the Trefftz-based methods generally yield ill-conditioned numerical models, and this precludes the use of iterative solvers, it is still possible to obtain sufficiently accurate solutions for engineering purposes using direct LU solvers [57].

3. Error indicator for the wave-based technique

In contrast to the element-based methods, the mathematical background of error estimation for Trefftz methods has been hardly researched yet. The error of the Trefftz solution is exclusively caused by the fact that the truncated wave function set does not satisfy the imposed boundary and

continuity conditions in a pointwise sense. In case of Trefftz methods, maximum principles can be valuable tools to asses domain errors for second-order elliptic partial differential equations. Roughly speaking, the strong maximum principle states that a function in a domain takes its maximum on the boundary of that domain and if a function achieves its maximum in the interior of the domain, the function is uniformly a constant. As no classical maximal principle holds for the Helmholtz equation [58], the solution should be bounded from the above in some norm by an appropriate norm of the boundary data [59]. In a similar way, the error of the Trefftz solution can be bounded by the error on the boundary, since the error field between the exact solution and the Trefftz solution also satisfies the Helmholtz equation, and no other error is present. Such bounds exist analytically for a limited class of problems, e.g., for elliptic second order PDEs, with certain boundary shapes and boundary conditions [60]. Most notably, a Max-Payne-Kuttler-Sigillito [60–62] bound has been applied [63] to the interior Helmholtz problem with Dirichlet boundary condition. This result has been further sharpened in [64, 65], and a similar bound for the least-squares Trefftz method including interface conditions has been also reported [66, 67]. It is still an open mathematical problem for practical benefits to generalize these results to Neumann, Robin and mixed boundary conditions, and unbounded Helmholtz problems.

In the wave-based technique, the accuracy of the approximation is merely determined by the size of the truncated wave function set. This paper introduces an error indicator rather than an estimator, in order to adaptively control the size of the wave function set for the pressure expansion. The error indicator evaluates the approximation error on the physical boundary and the continuity error between the subdomains, which requires the calculation of boundary integrals only. The error indicator can be then used to drive an adaptive strategy, which keeps the boundary errors below certain user-defined levels. Similar calculation schemes based on boundary error indicators were reported [68–70] for the inverse source method and the wave superposition method, for harmonic problems, where the classical maximum principle holds [71].

3.1. Relative L_2 norm boundary-error indicators for the physical boundary conditions and the continuity conditions

The applied error indicators evaluate the approximation error on the boundary, more exactly the deviation of the numerical solution from the prescribed boundary values and the continuity errors on the coupling interfaces in the relative L_2 norm. In case of the presented application-oriented model of the combustion engine, only normal velocity boundary condition is prescribed on the physical boundary part. In this context, the error indicators are defined only for the normal velocity boundary condition and the continuity conditions, for the sake of brevity. The definitions of the error indicators can be extended in a similar way for pressure and impedance boundary conditions as well.

Let us use the notation $\|\bullet\|_{2,\Gamma_\bullet} = \left\{ \int\limits_{\Gamma_\bullet} |\bullet|^2 \, \mathrm{d}\Gamma \right\}^{1/2}$ for the standard L_2-norm, $A_{\Gamma_\bullet} = \int\limits_{\Gamma_\bullet} \mathrm{d}\Gamma$ for the area of a given boundary surface and $\langle \bullet \rangle_{2,\Gamma_\bullet} = \left\{ \frac{1}{A_{\Gamma_\bullet}} \|\bullet\|^2_{2,\Gamma_\bullet} \right\}^{1/2}$ for an average L_2 norm value on a given boundary surface. Then let us introduce the definition

$$\langle \widetilde{v}_n \rangle_{2,\Gamma_v} = \left\{ \frac{1}{A_{\Gamma_v}} \|\overline{v}_n\|^2_{2,\Gamma_v} \right\}^{1/2}, \tag{10}$$

for the average L_2-norm prescribed normal velocity value on Γ_v.

Furthermore, let us use the notations

$$\begin{aligned}\left\langle \Delta\hat{p}^{(\alpha,\beta)}\right\rangle^2_{2,\Gamma_I^{(\alpha,\beta)}} &= \left\langle \widehat{p}^{(\beta)} - \widehat{p}^{(\alpha)}\right\rangle^2_{2,\Gamma_I^{(\alpha,\beta)}},\\ \left\langle \Delta\hat{v}_n^{(\alpha,\beta)}\right\rangle^2_{2,\Gamma_I^{(\alpha,\beta)}} &= \left\langle \widehat{v}_n^{(\alpha)} + \widehat{v}_n^{(\beta)}\right\rangle^2_{2,\Gamma_I^{(\alpha,\beta)}},\end{aligned} \tag{11}$$

for the average L_2 norm pressure and normal velocity coupling error on a coupling surface $\Gamma_I^{(\alpha,\beta)}$. Using the above definitions, we introduce the following local indicators:

$$\epsilon_v^{(\alpha)} = \frac{\left\langle \widehat{v}_n^{(\alpha)} - \overline{v}_n\right\rangle_{2,\Gamma_v^{(\alpha)}}}{\langle \widetilde{v}_n\rangle_{2,\Gamma}} \tag{12}$$

and

$$\epsilon_I^{(\alpha,\beta)} = \frac{\left\{\left\langle \Delta\hat{p}^{(\alpha,\beta)}\right\rangle^2_{2,\Gamma_I^{(\alpha,\beta)}} + \gamma^2\left\langle \Delta\hat{v}_n^{(\alpha,\beta)}\right\rangle^2_{2,\Gamma_I^{(\alpha,\beta)}}\right\}^{1/2}}{\left\{\left\langle \widehat{p}^{(\alpha)}\right\rangle^2_{2,\Gamma_I^{(\alpha,\beta)}} + \gamma^2\left\langle \widehat{v}_n^{(\alpha)}\right\rangle^2_{2,\Gamma_I^{(\alpha,\beta)}}\right\}^{1/2}}, \tag{13}$$

where $\epsilon_v^{(\alpha)}$ evaluates the relative L_2-norm velocity approximation error on $\Gamma_v^{(\alpha)}$ with respect to the L_2-norm average velocity value.

The error indicator $\epsilon_I^{(\alpha,\beta)}$ for the local continuity condition between $\Omega^{(\alpha)}$ and $\Omega^{(\beta)}$ expresses the coupling error as a combination of the L_2-norm pressure and velocity continuity error. The weighting of the norms of the pressure and normal velocity using the weighting term γ is similar to the definition of the interface continuity errors in the works [66, 67]. The weighting term γ is chosen to be equal to the coupling impedance Z_c of (8). In the context of this paper, the coupling impedance is equal to the characteristic impedance ($Z_c = \rho c$), which yields satisfactory accuracy [55].

In addition to the local indicators, let us define the global error indicator ϵ_v, which evaluates the velocity approximation errors on the corresponding boundary part Γ_v. Similarly, the indicator ϵ_I expresses the average relative L_2-norm continuity error, while ϵ_{I_U} evaluates the continuity error on the truncation sphere Γ_T

$$\epsilon_v = \frac{\langle \widehat{v}_n - \overline{v}_n\rangle_{2,\Gamma_v}}{\langle \widetilde{v}_n\rangle_{2,\Gamma_v}}, \tag{14}$$

$$\begin{aligned}\epsilon_I &= \frac{\left\{\sum\limits_{\alpha=1}^{N_\Omega}\sum\limits_{\beta=1}^{N_\Omega}\left\langle \Delta\hat{p}^{(\alpha,\beta)}\right\rangle^2_{2,\Gamma_I^{(\alpha,\beta)}} + \gamma^2\left\langle \Delta\hat{v}_n^{(\alpha,\beta)}\right\rangle^2_{2,\Gamma_I^{(\alpha,\beta)}}\right\}^{1/2}}{\left\{\sum\limits_{\alpha=1}^{N_\Omega}\sum\limits_{\beta=1}^{N_\Omega}\left(\left\langle \widehat{p}^{(\alpha)}\right\rangle^2_{2,\Gamma_I^{(\alpha,\beta)}} + \gamma^2\left\langle \widehat{v}_n^{(\alpha)}\right\rangle^2_{2,\Gamma_I^{(\alpha,\beta)}}\right)\right\}^{1/2}},\\ \epsilon_{I_U} &= \frac{\left\{\sum\limits_{\alpha=1}^{N_\Omega}\left\langle \Delta\hat{p}^{(\alpha,\Omega_U)}\right\rangle^2_{2,\Gamma_I^{(\alpha,\Omega_U)}} + \gamma^2\left\langle \Delta\hat{v}_n^{(\alpha,\Omega_U)}\right\rangle^2_{2,\Gamma_I^{(\alpha,\Omega_U)}}\right\}^{1/2}}{\left\{\sum\limits_{\alpha=1}^{N_\Omega}\left(\left\langle \widehat{p}^{(\alpha)}\right\rangle^2_{2,\Gamma_I^{(\alpha,\Omega_U)}} + \gamma^2\left\langle \widehat{v}_n^{(\alpha)}\right\rangle^2_{2,\Gamma_I^{(\alpha,\Omega_U)}}\right)\right\}^{1/2}}.\end{aligned} \tag{15}$$

The definitions of the global indicators are independent of the local indicators, and therefore they can be calculated independently. It is easy to follow from the above definitions that if the values of

the local indicators $\epsilon_v^{(\alpha)}$ and $\epsilon^{(\alpha,\beta)}$ are below their corresponding user-specified thresholds ϵ_v^* and ϵ_I^* for all α and β, then the values of the corresponding global indicators will be also below ϵ_v^* and ϵ_I^* respectively.

The aim of the present work is not to provide overall result quality indicators, but to present an adaptive local refinement approach to keep the boundary errors below certain user-defined thresholds. The presented error indicators provide information on the errors individually for the different boundary condition types. This allows flexible and individual control of each error type.

4. Adaptive calculation strategy

A definite advantage of WBT over element-based methods is that the domain subdivision (h-refinement) is usually kept fixed over the frequency range of interest, and the model refinement process involves only the enlargement of the wave function set (p-refinement). Utilizing this advantage, simple, but highly efficient refinement strategies can be adopted.

The implemented adaptive local refinement strategy uses both the global and the local error indicators. First, the global indicators of the boundary and continuity conditions are evaluated. If the global indicators exceed the user-defined thresholds, the local indicators will also be evaluated. In subdomains where any of the local indicators exceed the corresponding user-defined threshold the wave function set will be enlarged, and the numerical model will be recalculated until each global indicator satisfies the specified thresholds. In the next sections the investigated global and local refinement/wave function set control strategies are presented.

4.1. *A priori* frequency-dependent wave function truncation (global refinement)

In previous works on WBT, the highest spatial frequency component of the wave function set has been related to the physical wavelength. In other words, the size of the wave function set was *a priori* controlled by the calculation frequency and a user defined truncation parameter [38, 49, 55].

Based on the assumption that the highest spatial frequency component of the wave functions can be related to the given acoustic wavelength λ, the following *a priori* truncation rules can be adopted:

$$N_x^{(\alpha)} = \frac{T_{WF}}{\lambda} L_x^{(\alpha)}, \qquad N_y^{(\alpha)} = \frac{T_{WF}}{\lambda} L_y^{(\alpha)}, \qquad N_z^{(\alpha)} = \frac{T_{WF}}{\lambda} L_z^{(\alpha)}, \tag{16}$$

where T_{WF} is an arbitrary global truncation parameter and $N_x^{(\alpha)}$, $N_y^{(\alpha)}$ and $N_z^{(\alpha)}$ refer to the integer parameters of the bounded wave function set (4) (rounded to the nearest integer value). Practically, a truncation factor $T_{WF} = 2$ means that wave functions whose wavelength λ_w of the highest oscillatory cosine function of the wave function set in a given direction is smaller than or about equal to the physical wavelength ($\lambda_w \leq \lambda$). As a result, the highest oscillatory k-components of the wave function set are approximately equal in each directions: with a given value of T_{WF}, $\max(k_{x_{w\bullet}}^{(\alpha)}) \approx \max(k_{y_{w\bullet}}^{(\alpha)}) \approx \max(k_{z_{w\bullet}}^{(\alpha)})$ for all α, apart from the rounding of $N_x^{(\alpha)}$, $N_y^{(\alpha)}$, $N_z^{(\alpha)}$ to the nearest integers. The expression (16) implements a frequency dependent, homogeneous enlargement (global refinement) of the wave function set in all domains.

A similar, frequency-dependent *a priori* truncation rule has been applied in [42] to the radiation function set in the unbounded domain Ω_U. The order of the radiation function set, which is determined by the upper bound N_{RF} in the summation (6), can be set according to

$$N_{RF} = 2R_T T_{RF} k, \tag{17}$$

where R_T is the radius of the truncation sphere, k is the wavenumber and T_{RF} is an arbitrary truncation parameter.

4.2. Wave function truncation for the adaptive calculation strategy (local refinement)

For the adaptive local refinement scheme, two different truncation rules for the wave function sets are presented. First, a domainwise frequency-independent truncation rule is shown, in which the initial number of wave functions is independent of the calculation frequency and the wave function set is *a posteriori*, iteratively increased until the prescribed error indicator thresholds are achieved. Second, a combined *a priori/a posteriori* wave function control is shown, in which the initial wave function set size is dependent on the frequency, and is domainwise enlarged by local refinement,if needed.

4.2.1. Frequency-independent a posteriori control (recalculate from scratch approach)

The domainwise frequency-independent truncation of the wave function set is implemented according to the following expression:

$$N_x^{(\alpha)} = M^{(\alpha)} \frac{N_{\Omega^B} L_x^{(\alpha)}}{\sum_{\alpha=1}^{N_{\Omega^B}} L_x^{(\alpha)}}, \qquad N_y^{(\alpha)} = M^{(\alpha)} \frac{N_{\Omega^B} L_y^{(\alpha)}}{\sum_{\alpha=1}^{N_{\Omega^B}} L_y^{(\alpha)}}, \qquad N_z^{(\alpha)} = M^{(\alpha)} \frac{N_{\Omega^B} L_z^{(\alpha)}}{\sum_{\alpha=1}^{N_{\Omega^B}} L_z^{(\alpha)}}, \tag{18}$$

where the value of $M^{(\alpha)}$ controls the truncation of the wave function set, and the integers $N_x^{(\alpha)}$,$N_y^{(\alpha)}$,$N_z^{(\alpha)}$ are independent of the calculation frequency, but proportional to the corresponding dimensions of the domain $\Omega^{(\alpha)}$. Similarly to the result of (16), with a given value of $M^{(\alpha)}$, $\max(k_{x_{w\bullet}}^{(\alpha)}) \approx \max(k_{y_{w\bullet}}^{(\alpha)}) \approx \max(k_{z_{w\bullet}}^{(\alpha)})$ for all α, apart from the rounding of $N_x^{(\alpha)}$,$N_y^{(\alpha)}$,$N_z^{(\alpha)}$ to the nearest integers.

The initial number of wave functions in the first calculation is determined by a user-defined initial value of $M^{(\alpha)}$, and hence the initial number of wave functions is independent of the calculation frequency. The value of $M^{(\alpha)}$ is iteratively enlarged in the successive recalculation steps in the indicated domains, until the prescribed boundary error tolerances are satisfied. Therefore, this control strategy implements a full *recalculate from scratch approach* for the purpose of the iterative local refinement, since at each frequency step, the adaptation restarts from the initial wave function configuration.

For the adaptation of the expansion set in the unbounded domain Ω_U, the highest order of the radiation functions is controlled by the value of the upper bound N_{RF} in (6).

4.2.2. Combined a priori/a posteriori control

As an alternative to the full restart from scratch approach, a control rule using a frequency-dependent (*a priori*) initial number of wave functions is also applied. The frequency-dependent initial wave function set is configured by means of the *a priori* truncation rules (16) and (17) and refined according to (18). The combined *a priori/a posteriori* wave function control for a subdomain $\Omega^{(\alpha)}$ in the bounded part Ω_B is thus formalized as follows:

$$\begin{aligned} N_x^{(\alpha)} &= \frac{T_{WF}^0}{\lambda} L_x^{(\alpha)} + M^{(\alpha)} \frac{N_{\Omega^B} L_x^{(\alpha)}}{\sum_{\alpha=1}^{N_{\Omega^B}} L_x^{(\alpha)}}, \qquad N_y^{(\alpha)} = \frac{T_{WF}^0}{\lambda} L_y^{(\alpha)} + M^{(\alpha)} \frac{N_{\Omega^B} L_y^{(\alpha)}}{\sum_{\alpha=1}^{N_{\Omega^B}} L_y^{(\alpha)}}, \\ N_z^{(\alpha)} &= \frac{T_{WF}^0}{\lambda} L_z^{(\alpha)} + M^{(\alpha)} \frac{N_{\Omega^B} L_z^{(\alpha)}}{\sum_{\alpha=1}^{N_{\Omega^B}} L_z^{(\alpha)}}, \end{aligned} \tag{19}$$

where T^0_{WF} is an initial, global *a priori* truncation parameter. For the unbounded part, the combined control strategy was similarly formalized as

$$N_{RF} = 2R_T T^0_{RF} k + N, \tag{20}$$

where T^0_{RF} is an initial, *a priori* truncation parameter and N is the value increased by the adaptive strategy.

4.2.3. Acceleration of the iterative process

During the assembly of the system matrix, it is possible to reuse matrix blocks of subdomains whose wave function set was not enlarged after the previous recalculation step. If the wave function set in a subdomain $\Omega^{(\alpha)}$ is not enlarged in a given recalculation step, the corresponding matrix block [55] will not change, and does not need to be recalculated. If subdomains $\Omega^{(\alpha)}$ and $\Omega^{(\beta)}$ are adjacent sharing a common coupling interface, and the wave function set is not enlarged in neither of them, then the corresponding coupling matrix blocks [55] does not need to be recalculated either. For the acceleration of the iterative recalculations the presented implementation uses disk caching. However, it is not possible to reuse matrix blocks from a previous frequency step, since the system matrix of WBT is frequency-dependent.

4.3. A wave function-dependent numerical integration scheme

Due to the poor numerical conditioning of the WBT models, the accuracy of the numerical integration needs to be of the order of the machine precision. It has been shown that the classical Gauss-Legendre quadrature is applicable for the evaluation of the oscillatory integrals appearing in the WBT formulations [72]. A fixed high number of integration points would however degrade the computational performance of the method. In order to guarantee a high integration accuracy and possibly fast numerical integral evaluation, the size of the integration quadrature should be scaled by the order of the oscillatory wave functions and the integration area. Numerical trials were carried out to derive a suitable control rule for the integration quadrature. The WBT model variants of the engine (see Sec. 6) were calculated with various truncation radii in the range of $R_T = 0.55\,\mathrm{m} \ldots 0.8\,\mathrm{m}$. Each model version was calculated by iteratively increasing $M^{(\alpha)}$ from 1 up to 14 for all $\Omega^{(\alpha)}$. At each value of $M^{(\alpha)}$, N_{RF} was also increased from 1 up to 70. At each iteration step, the size of the integration quadrature of the individual integration surfaces was increased, until the changes in the numeric values of the matrix coefficients were below an absolute and relative tolerance scheme. The condition, commonly used in adaptive quadrature algorithms [73],

$$||a^{(n+1)}_{i,j} - a^{(n)}_{i,j}|| < \max\left(\tau_{abs}, a^{(n+1)}_{i,j}\tau_{rel}\right) \tag{21}$$

had to be satisfied for all i, j, where $a_{i,j}$ is a coefficient of the system matrix. The $a^{(n+1)}_{(i,j)}$ stands for the coefficient calculated by the increased quadrature size, while $a^{(n)}_{(i,j)}$ denotes the coefficient calculated by the previous quadrature size. The absolute tolerance was $\tau_{abs} = 10^{-15}$ and the relative tolerance was $\tau_{rel} = 10^{-15}$. These values were found to provide the highest possible accuracy without leading to uncontrollable growth of the quadrature sizes during the numerical trial. For each surface, the quadrature size that satisfied the above tolerance scheme was correlated with the highest k-component of the corresponding wave function set and the area of the given surface. The relation was sought in the form of a simple linear expression:

$$N^{(\Gamma^{(\alpha)}_\bullet)}_{\mathrm{Gauss}} = A \max\left(|k^{(\alpha)}_{x_{w\bullet}}|, |k^{(\alpha)}_{y_{w\bullet}}|, |k^{(\alpha)}_{z_{w\bullet}}|\right) L^{\Gamma^{(\alpha)}_\bullet}_{\max} + B, \tag{22}$$

where $N_{\text{Gauss}}^{(\Gamma_\bullet^{(\alpha)})}$ denotes the number of the 1D Gaussian points, and it results in $N_{\text{Gauss}}^{(\Gamma_\bullet^{(\alpha)})} \times N_{\text{Gauss}}^{(\Gamma_\bullet^{(\alpha)})}$ Gaussian points on a general 3D integration surface. $L_{\text{max}}^{\Gamma_\bullet^{(\alpha)}}$ is the length of the longest edge of the given surface $\Gamma_\bullet^{(\alpha)}$. This model relates the number of integration points to the highest oscillatory component of the wave functions in the given domain and to the size of the integration area in a simple manner.

For the integration on the spherical surface sectors of the truncation sphere Γ_T, the following linear model was applied:

$$N_{\text{Gauss}}^{(\Gamma_{T_i})} = F\ N_{RF} + G\theta_{\Gamma_{T_i}} + H\theta_{\Gamma_{T_i}} N_{RF} + I, \tag{23}$$

where $\theta_{\Gamma_{T_i}}$ is the largest central angle corresponding to the spherical surface section Γ_{T_i}. The parameters values of $A = 1$, $B = 20$, $F = 0.035$, $G = 35$, $H = 0.2$ and $I = 10$ were determined by fitting a conservative upper bound to the registered data. Since the subdomains of the presented model variants have relatively various shapes and dimensions, the given values of A, B, F, G, H and I are expected to provide appropiate quadrature sizes for similar sized problems, e.g., passenger car combustion engine models with similar dimensions and frequency range of interest. For practical computational time/effort considerations, the maximal quadrature size was limited to 100×100 points per integration surface.

5. Definition of a combustion engine structural model

In order to verify the proposed adaptive calculation strategy in a simulation of a realistic engine sound field, an application-oriented structural model of a four-cylinder inline gasoline engine was created. Both for WBT and BEM, simplified surrogate acoustic boundaries were created, which are typically not coincident with the surface of the structure for efficiency reasons and because of potential holes in the structural mesh. The shape of the engine block was simplified in the present work, and auxiliaries of the engine were omitted. The simplified structure allowed creating surrogate acoustic boundaries, which are close to the surface, but efficient for WBT modelling, consisting of planar surfaces only.

The geometric definition of the wave-based models in the present work was made by hand. The combustion engine structural model was created by means of the commercial engine simulation software AVL EXCITE. The external forces acting on the engine system are gas pressures at 4000 rpm, full load and at an output torque of 226 Nm. The condensed FE models of the engine block, the crankshaft and the conrods are valid up to 3 kHz, and so are the concentrated masses of the pistons. The contact forces between the involved bodies and suspensions are described by force models that show realistic response in the investigated frequency range [74, 75]. The main bearings (cylindrical rings in Fig. 2) are described by an enhanced hydrodynamic model [76]. The piston-liner contact (bundle of thin lines from the top of the conrod to the liner contact nodes) is described by an empirical force formulation. A multi-body-simulation (using the software AVL EXCITE) was performed to obtain the structural dynamics of the engine. The velocities were recovered onto the surface of the engine and transformed into frequency domain at the relevant engine orders. The resulted velocity boundary condition set is defined from 204.188 Hz up to 2994.73 Hz with a frequency step of 34.031 Hz (total of 83 frequency steps). The exact frequency values are displayed rounded to the nearest integer in the text from here on, for the sake of shorthand notation. The normal velocity boundary condition distribution is depicted in Fig. 3 at selected frequencies. The structural velocity data has been applied as a normal velocity (Neumann) boundary condition in the radiation model. Therefore, the prescribed structural normal velocity boundary condition represents a one-way structural-fluid coupling.

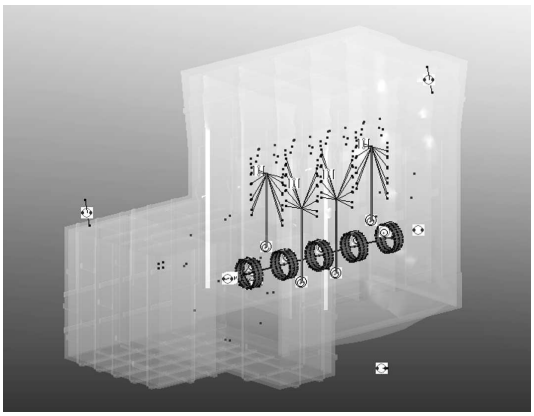

Fig. 2. Picture of the MBS model from AVL Excite.

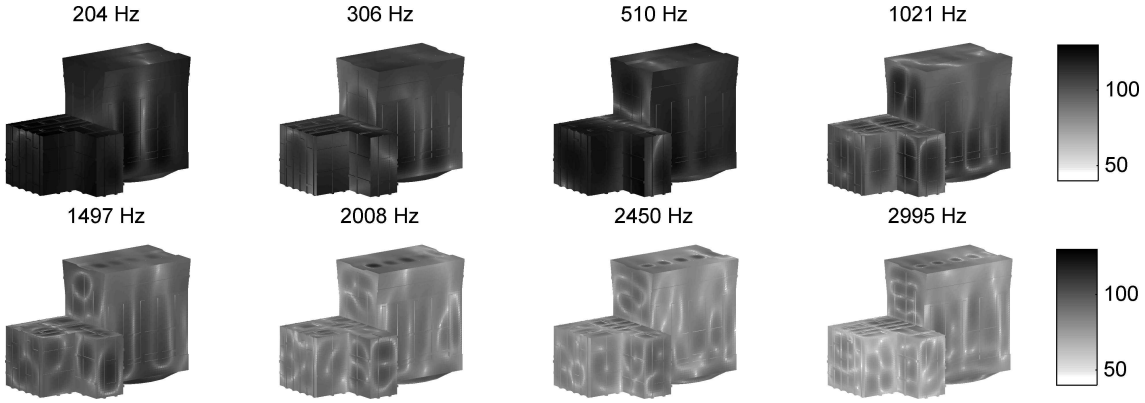

Fig. 3. Magnitude of structural normal velocity distribution at selected frequencies in $\mathrm{dB}_{re\ 10^{-9}\ \mathrm{m/s}}$ according to ISO 1683.

6. Engine sound radiation model

6.1. Definition of the numerical model in WBT and its BE reference model

Consider the radiating engine boundary depicted in Fig. 3 with its main dimensions of 419×759×495.2 mm. Two model variants of the free-field engine radiation model were created, depicted in Fig. 4. The first variant contains 9 subdomains in the bounded part Ω_B ($N_\Omega = 10$), while the second has 32 subdomains ($N_\Omega = 33$). The topology of subdomains of the second model variant ($N_\Omega = 33$) ensures that no abrupt change of boundary conditions (or jump in the boundary conditions) occurs on the planar boundaries of the subdomains, but such changes occur only at

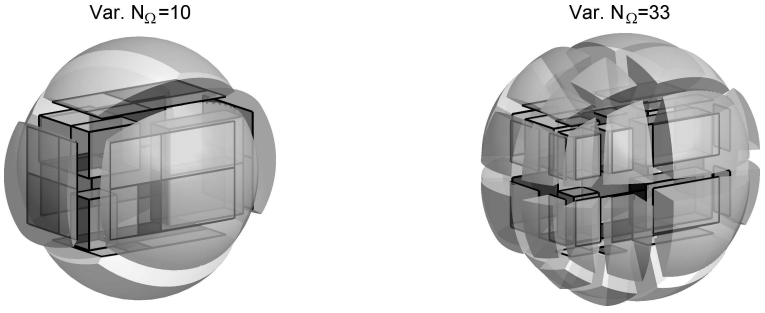

Fig. 4. Topology overview of two model variants $N_\Omega = 10$ and $N_\Omega = 33$ of engine radiation model.

interfaces between two subdomains. This condition is preferable for WBT, since the approximation of such jumps within one subdomain requires an excessive amount of wave functions, which deteriorates the performance of the numerical model. The influence of the modelling topology and the number of subdomain will be analysed in the next section.

For verification of the WBT results, a very fine BE mesh of the surrogate acoustic boundary was created. The BE mesh has a maximal element length of 10 mm, and the mesh is valid up to 3378 Hz, considering a $\lambda/10$ element length rule. The BE mesh consists of 14 118 nodes and 14 116 elements. Since the engine radiation model has a closed boundary, the direct BE formulation could be used. The effect of the so-called irregular frequencies (the eigenfrequencies corresponding to the domain inside the closed model boundary) could be efficiently mitigated by randomly located overdetermination points.

The structural velocity distribution (depicted in Fig. 3) was mapped to the nodes of the BE mesh using an inverse distance weighted (IDW) mapping approach, in which the complex velocity vector of the i-th node of the BE mesh is calculated as a linear combination of the velocity vectors of the 8 closest nodes of the engine FE mesh:

$$v(\mathbf{r}_i)_{\mathrm{BE}} = \sum_{j=1}^{8} \frac{1}{d_j} v(\mathbf{r}_j)_{\mathrm{FE}}, \tag{24}$$

where

$$d_j = ||\mathbf{r}_i - \mathbf{r}_j|| \tag{25}$$

is the distance between the i-th BE node, and the j-th structural FE node, and b is a factor such that

$$b \sum_{j=1}^{8} \frac{1}{d_j} = 1. \tag{26}$$

In order to guarantee that both the WB model and the BE model obtain the same normal velocity boundary condition, the nodal values of the normal velocity boundary condition of the BE model ($v(\mathbf{r}_i)_{\mathrm{BE}}$) were interpolated to the Gauss-integration points of the coincident WBT model surfaces. For the interpolation from the BE nodes to the integration points, the same IDW mapping has been applied.

The approximation error of WBT with respect to the reference BE calculation is expressed as a relative L_2 norm pressure error at a distance of 1m from the engine (the numerical integration on the $R = 1$ m spherical surface has been carried out by means of a 9600-points Gauss-quadrature).

$$\epsilon_{\mathrm{BEM-WBT}} \approx \left\{ \frac{\displaystyle\int_{R=1\mathrm{m}} |\widehat{p}(\mathbf{r}) - p_{\mathrm{BEM}}(\mathbf{r})|^2 \, \mathrm{d}\Gamma}{\displaystyle\int_{R=1\mathrm{m}} |p_{\mathrm{BEM}}(\mathbf{r})|^2 \, \mathrm{d}\Gamma} \right\}^{1/2}. \tag{27}$$

If $\widehat{p}(\mathbf{r})$ in Ω_U satisfies the Sommerfeld condition, then $\displaystyle\int_{R\to\infty} |\widehat{p}(\mathbf{r})|^2 \, \mathrm{d}\Gamma = \text{const.}$ [77]. Thus, (27) is a well-suited measure of the approximation error in the exterior domain.

The reference BE model was created and calculated in the SYSNOISE Rev. 5.6 commercial BEM package with 100 randomly generated overdetermination points. The WBT code was implemented and run in MATLAB R2011b. Both the BEM and the WBT calculations were performed on the same AMD 3.0 GHz CPU with 16 Gb RAM. The BE reference model was solved in approx. 11 minutes per frequency step and the post-processing of the 9600 response points took approx. 6 minutes per frequency step. Therefore, the total calculation time of the BE modal was 913 minutes without post-processing, and 1411 minutes with post-processing. The post processing of the WBT results took at most 10 seconds per frequency for the 9600 response points.

6.2. Results

6.2.1. Convergence behaviour of model variants

Figure 5 shows the convergence behaviour of the two model variants of the free-field engine radiation case at a selected frequency of 2484 Hz. The values of the global indicators (ϵ_v, ϵ_I, ϵ_{I_U}) and the approximation accuracy $\epsilon_{\text{BEM}-\text{WBT}}$ are plotted against the number of DOFs. The approximation error is also plotted against the calculation time, in order to show the computational effort needed to calculate the different model variants. Furthermore, the number of DOFs is depicted against the calculation time, which is useful to explain the computational efficiency of the different modelling topologies.

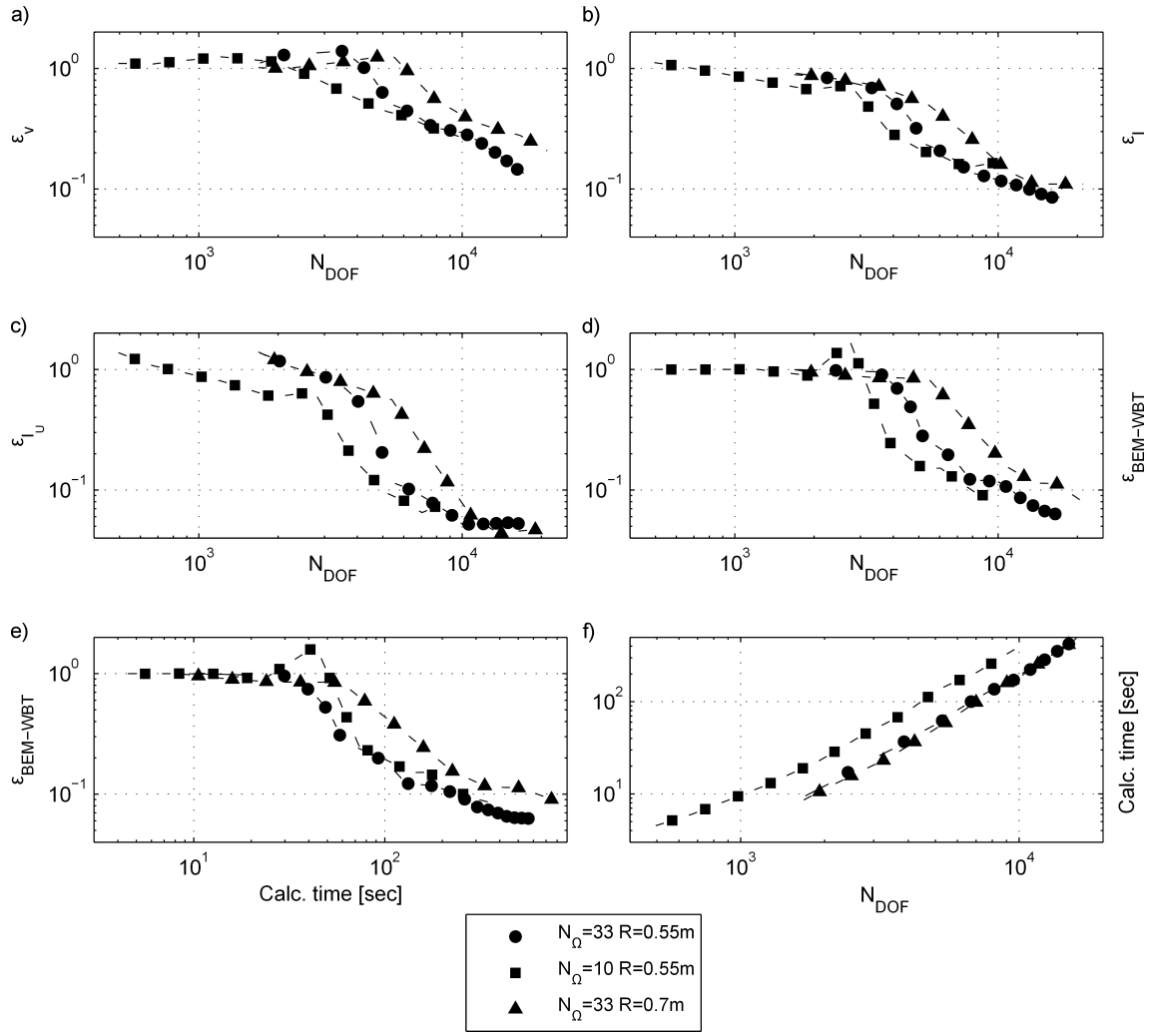

Fig. 5. Convergence properties of the engine radiation model variants ($N_\Omega = 33$, $R = 0.55$ m, $N_\Omega = 10$, $R = 0.55$ m and $N_\Omega = 33$, $R = 0.7$ m) at 2484 Hz: Values of the boundary-error indicators: a) ϵ_v, b) ϵ_I, c) ϵ_{I_U} vs. the number of degrees of freedom, the relative L_2-norm approximation error with respect to the BEM reference ($\epsilon_{\text{BEM-WBT}}$) vs. the number of degrees of freedom (d) and vs. calculation time (e), and calculation time vs. the number of degrees of freedom (f).

The variant $N_\Omega = 10$ was calculated with a truncation radius of 0.55 m, while the variant $N_\Omega = 33$ was calculated with truncation radii 0.55 m and 0.7 m. The convergence plot was obtained by a homogeneous enlargement of the wave function set using the wave function control expression (18). The initial values of $M^{(\alpha)}$ were set to $M^{(\alpha)} = 1$ for all α, and $M^{(\alpha)}$ was increased by a value of 1 for all domains at each recalculation step. The initial order of the radiation functions N_{RF} was set

to $N_{RF} = 2$ and was increased by a value of 6 at each recalculation step. The recalculations were stopped, if any of the error indicators, or the approximation accuracy $\epsilon_{\mathrm{BEM-WBT}}$ showed no more improvement. The reason for the lack of improvement at the last recalculation steps is twofold. The imposed velocity boundary condition on the surrogate acoustic boundary is an artificially mapped non-smooth boundary data, which needs very high oscillatory orders to describe accurately. Since the numerical integrals are evaluated by a finite integration quadrature size (see Subsec. 4.3), thus numerical instabilities in the solution of the ill-conditioned linear system are inevitable at such high oscillatory orders. Therefore, Fig. 5 depicts results of the 7–10 successive refinement iterations depending on the model size.

As depicted in Fig. 5, the approximation accuracy $\epsilon_{\mathrm{BEM-WBT}}$ approaches to a value of 0.05 at the final recalculation steps. At the selected frequency, it is clearly visible that the numerical model with the larger radius of 0.7 m requires more DOFs and, as a result, longer calculation times than the variants with the smaller truncation radii. From Fig. 5d it appears that the variant $N_\Omega = 10$ is the most efficient, if the approximation error is seen only against the number of DOFs. The efficiency of the variant $N_\Omega = 10$ (in terms of the number of DOFs) is not reflected however in the corresponding calculation times in Fig. 5e. The jumps of boundary conditions within the subdomains of the model variant $N_\Omega = 10$ require high-order wave functions, which deteriorate the computational efficiency, since the higher-order wave functions require more accurate numerical integration. Observing the number of DOFs in relation to the calculation time in Fig. 5f, it can be seen that the variant $N_\Omega = 33$ is more efficient to calculate, since the same number of DOFs is calculated at a lower computational time; the lower number of DOFs of the $N_\Omega = 10$ variant can not compensate the efficiency advantage of the $N_\Omega = 33$ variant. As a consequence, the variant with the higher number of subdomains ($N_\Omega = 33$) was chosen for further calculations. Efficiency and consistency of the global error indicators with the solution error ($\epsilon_{\mathrm{BEM-WBT}}$) can also be assessed from Fig. 5. The convergence behavior of the error indicators is consistent with the solution error. The solution error shows the highest correlation with the coupling error indicators ϵ_I and ϵ_{I_U}, while ϵ_v overestimates the error. An engineering accuracy of 5% was achieved with $\epsilon_v = 0.12$.

6.2.2. Aim of comparison and focus of investigation

For the analysis of the adaptive calculation strategy and the error indicators, a limited number of calculation parameters and error indicator thresholds were set up and investigated. Results from the adaptive strategy were calculated with both the frequency-independent wave function control (full restart from scratch approach) and the combined *a priori/a posteriori* wave function control. Results of the adaptive strategy were compared with results of the *a priori*, frequency dependent, global refinement presented in Subsec. 4.1. The primary focus of the investigation was to obtain results with an engineering accuracy of approx. 10%. The solution error was expressed in terms of the relative L_2-norm pressure error defined in (27).

6.2.3. Selection of threshold settings

For the adaptive calculation strategy, the thresholds of the error indicators were defined in such a way that $\epsilon_v^* \geq \epsilon_I^* \geq \epsilon_{I_U}^*$, where ϵ_v^*, ϵ_I^* and $\epsilon_{I_U}^*$ denote the prescribed threshold values for ϵ_v, ϵ_I, ϵ_{I_U} respectively. The presumption behind the selection of this threshold scheme is that it is preferred that the accuracy of the numerical solution is governed by the error in the physical boundary conditions, rather than by the error in the interface continuity conditions. This results in a smoother, more continuous pressure field, with fewer artifacts at the coupling interfaces. In other words, the resulted dynamic pressure field behaves more like a global solution, rather than a set of roughly coupled domainwise solutions. Moreover, it is beneficial to set the indicator thresholds such, that $\epsilon_I^* > \epsilon_{I_U}^*$, since the more restricted continuity error in the unbounded domain only implies the enlargement of the radiation function set, which does not considerably increase the total number of DOFs, but generally leads to higher accuracy in the exterior domain.

On the other hand, the resulting error indicator values are not independent of each other, e.g., a very restricted continuity error level will have an influence on the physical boundary errors as well (and vice versa), and hence certain threshold value combinations does not lead to significantly different results. Furthermore, the selection of the increase steps of $M^{(\alpha)}$ and N_{RF} for a possibly optimal number of recalculations (i.e., minimal number of recalculations, yet avoiding over-refinement) also have the consequence that small changes of the threshold settings do not lead to remarkable changes in the indicator values and the approximation error. With all these in mind, the boundary error thresholds were defined in the range of 0.1–0.5 to obtain a brief parametric analysis.

6.2.4. A priori, frequency-dependent global refinement results

Results of the *a priori* frequency-dependent global refinement were evaluated in the range of $T_{WF} = 1 \ldots 4$ with $T_{RF} = 1$. The same parameter set of T_{WF} with $T_{RF} = 2$ did not improve the accuracy remarkably, but increased the calculation times significantly. Moreover the expression (17) with $T_{RF} = 2$ yields a radiation function set order of $N_{RF} = 85$ with the truncation radius of $R_T = 0.55$ m approx. at 2109 Hz. Above this order, the calculation of spherical Hankel functions is numerically unstable (instabilities associated with the calculation of the spherical Hankel functions for large orders are extensively reported in the FMM (fast multipole method) literature, see, e.g., [78, 79]).

Table 1 provides an overview of the numerical values and the right column of Fig. 6 depicts the results in the calculation frequency range. The global *a priori* truncation factors of $T_{WF} = 1$ and $T_{WF} = 2$ provide unreliable results from practical viewpoint, with maximal $\epsilon_{\mathrm{BEM-WBT}}$ error

Table 1. Results of the *a priori*, frequency-dependent global truncation rules. Contents of the table are the following: the solution error $\epsilon_{\mathrm{BEM-WBT}}$, total calculation time, number of DOFs in Ω_B and Ω_U, the values of the global indicators ϵ_v, ϵ_I and ϵ_{I_U}. Numerical values are provided as minimum, maximum and average values in the calculation frequency range, and as actual values at the example frequency steps of 510 Hz, 1497 Hz and 2484 Hz.

Setting	$\epsilon_{WBT-BEM}$	Time [min.]	$N_{DOF}^{\Omega_B}$	$N_{DOF}^{\Omega_U}$	ϵ_v	ϵ_I	ϵ_{I_U}
$T_{WF} = 1$, $T_{RF} = 1$	0.131–1.207	357.88	1674–3002	25–3721	0.288–1.658	0.237–0.726	0.166–0.706
Average:	0.691				0.954	0.518	0.486
510 Hz	0.178	0.27	1674	121	0.365	0.264	0.218
1497 Hz	0.966	1.65	1810	961	1.043	0.605	0.593
2484 Hz	1.155	9.00	2262	2601	1.658	0.699	0.576
$T_{WF} = 2$, $T_{RF} = 1$	0.131–0.743	439.08	1674–8502	25–3721	0.288–0.964	0.185–0.461	0.106–0.486
Average:	0.274				0.534	0.256	0.202
510 Hz	0.175	0.25	1686	121	0.359	0.261	0.215
1497 Hz	0.366	1.94	3002	961	0.731	0.297	0.140
2484 Hz	0.288	11.16	6060	2601	0.641	0.241	0.124
$T_{WF} = 3$, $T_{RF} = 1$	0.070–0.257	768.25	1674–17214	25–3721	0.147–0.527	0.073–0.351	0.037–0.486
Average:	0.126				0.285	0.140	0.102
510 Hz	0.160	0.28	1810	121	0.319	0.214	0.160
1497 Hz	0.105	3.15	5234	961	0.249	0.121	0.071
2484 Hz	0.127	19.02	12438	2601	0.241	0.101	0.050
$T_{WF} = 4$, $T_{RF} = 1$	0.053–0.189	1691.88	1674–29212	25–3721	0.109–0.456	0.056–0.308	0.033–0.401
Average:	0.093				0.198	0.175	0.183
510 Hz	0.140	0.33	2036	121	0.269	0.195	0.145
1497 Hz	0.075	5.26	8502	961	0.163	0.080	0.047
2484 Hz	0.085	38.21	20818	2601	0.140	0.071	0.043

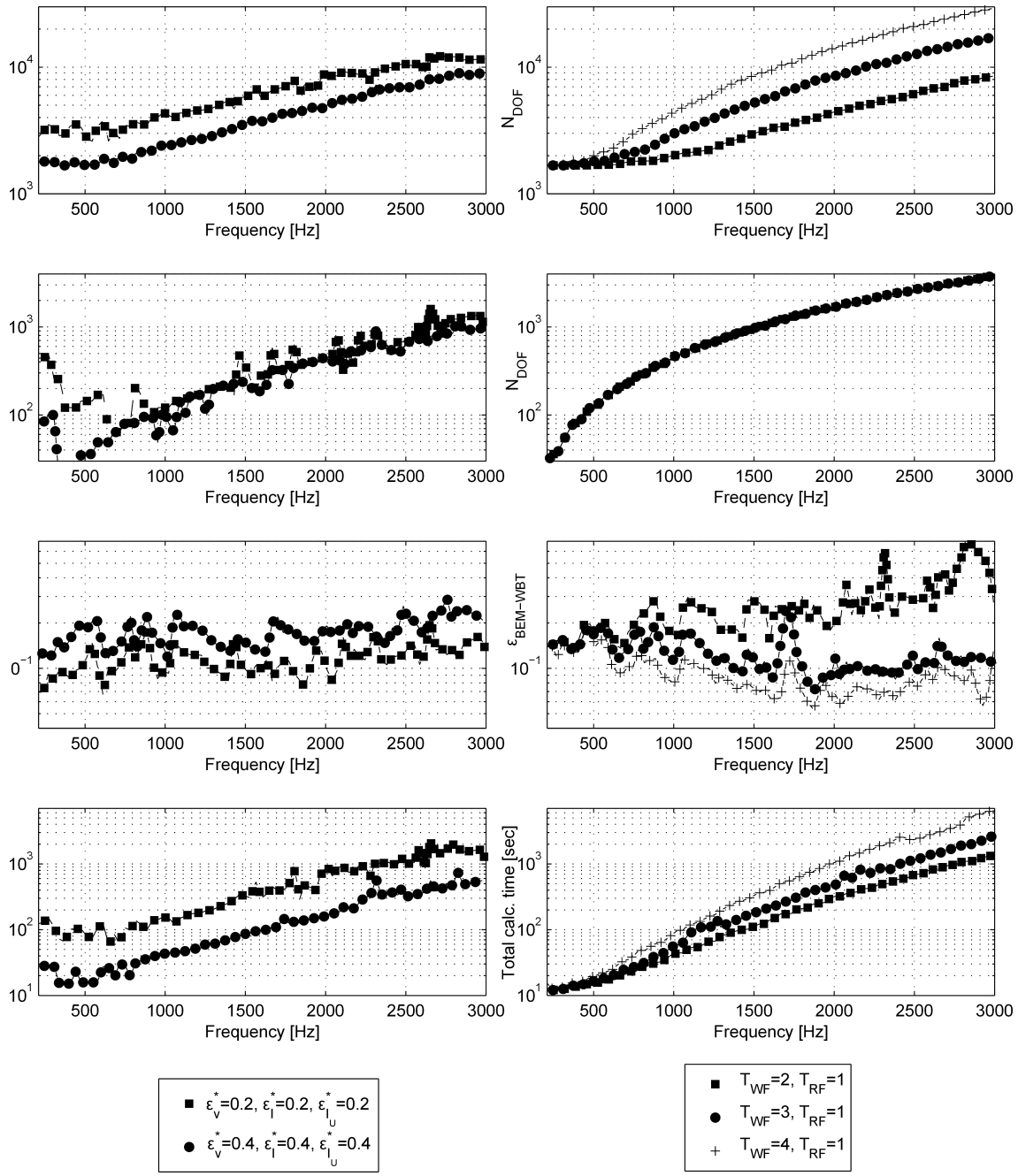

Fig. 6. Comparison of results obtained by the combined *a priori/a posteriori* adaptive strategy (adaptive local refinement, first column) and the *a priori* frequency dependent wave-function strategies (global refinement, second column). Depicted: Number of DOFs in Ω_B (first row), number of DOFs in Ω_U (second row), solution error with respect to the BEM reference (third row), calculation time per frequency (fourth row). Calculation times for the adaptive strategy represent the total time spent on the recalculations to satisfy the prescribed indicator thresholds.

levels of 1.207 and 0.743 respectively. With $T_{WF} = 1$ the error is very high at 1500 Hz, already increasing excessively above 1000 Hz. The result of $T_{WF} = 2$ still exhibits increasing error level above 1500 Hz. These results immediately suggest that a constant truncation factor value does not necessarily lead to controlled accuracy levels. The truncation factor of $T_{WF} = 3$ provides an average accuracy of 0.126 in 768 minutes in the calculated frequency range, which was chosen as a reference for calculation cost/accuracy compromise with approx. 10% accuracy goal for comparison with the adaptive strategy. $T_{WF} = 4$ further improves the result of $T_{WF} = 3$ with the average error being

less than 10% (0.093) at a cost of significantly high calculation time of 1691 minutes. Both for $T_{WF} = 3$ and for $T_{WF} = 4$, it is apparent that the error is decreasing with increasing frequency, in other words the error is higher at low frequency. In fact, the value of the truncation factor T_{WF} has a low effect on the number of DOFs in Ω_B (and as a result on the accuracy) in the low frequency range. The change of the truncation parameter from $T_{WF} = 2$ to $T_{WF} = 4$ only increases the number of DOFs in Ω_B from from 1686 to 2036 at 510 Hz. However, at 2484 Hz the number of DOFs increases excessively, from 8502 to 29 212 with $T_{WF} = 2$ to $T_{WF} = 4$.

6.2.5. Results of the frequency-independent, a posteriori control (full restart from scratch approach)

To compare results of the adaptive recalculate from scratch strategy with results of the frequency-dependent global refinement, first we analyze equal threshold settings in the form of $\epsilon_v^* = \epsilon_I^* = \epsilon_{I_U}^*$. The parameters of the wave function control rule (18) were set up such, that the initial values of $M^{(\alpha)}$ were set to $M^{(\alpha)} = 1$, with a minimal value of $N_x = N_y = N_z = 2$ for all α, and $M^{(\alpha)}$ was increased by a value of 1, if necessary. The initial order of the radiation functions was set to $N_{RF} = 2$ and was increased by a value of 6, if necessary.

Table 2 provides an overview of the numerical results of the calculations. The settings of $\epsilon_v^* = \epsilon_I^* = \epsilon_{I_U}^* = 0.5$ and $\epsilon_v^* = \epsilon_I^* = \epsilon_{I_U}^* = 0.4$ provide very appealing calculation times, with total calculation times of 355.98 minutes and 426 minutes, respectively. The error of these settings lies however in the range of 0.07–0.5 and 0.07–0.4 respectively. It is apparent, that the maximal values of the solution error $\epsilon_{\text{BEM}-\text{WBT}}$ approach the value of the prescribed boundary error thresholds. Both the average indicator values and the average solution error are however well below (with a factor of 2) the corresponding indicator thresholds. Since, the increase steps of $M^{(\alpha)}$ and N_{RF} were selected to maintain a possibly low number of recalculations while avoiding over-refinement as much as possible, approaching the prescribed thresholds is not achievable in fine steps, and as such, the error levels may drop well below the prescribed thresholds after a given refinement step. The accuracy of results obtained by the settings of $\epsilon_v^* = \epsilon_I^* = \epsilon_{I_U}^* = 0.3$ and $\epsilon_v^* = \epsilon_I^* = \epsilon_{I_U}^* = 0.2$ are indeed very close to each other. However, restriction of the velocity error indicator ϵ_v to 0.2 increased the total calculation time significantly (to 1023 minutes) and resulted in an average $\epsilon_{\text{BEM}-\text{WBT}}$ error level of 0.124. Table 2 also includes results of the threshold setting $\epsilon_v^* = \epsilon_I^* = \epsilon_{I_U}^* = 0.1$. Restriction of the normal velocity boundary error indicator ϵ_v below the value of 0.1 was however not achievable in the full frequency range of interest, as the indicator values stagnated in the range of 0.1–0.15, as also seen in the convergence analysis plots in Fig. 5 in Subsec. 6.2.1. Therefore, consistent calculation times can not be indicated for this parameter case.

Table 3 presents results of calculations obtained by threshold settings $\epsilon_v^* > \epsilon_I^* > \epsilon_{I_U}^*$. By definition, the settings of $\epsilon_v^* = 0.5, \epsilon_I^* = 0.4, \epsilon_{I_U}^* = 0.3$ and $\epsilon_v^* = 0.4, \epsilon_I^* = 0.3, \epsilon_{I_U}^* = 0.2$ and $\epsilon_v^* = 0.3, \epsilon_I^* = 0.2, \epsilon_{I_U}^* = 0.1$ provide lower solution error than the settings of $\epsilon_v^* = \epsilon_I^* = \epsilon_{I_U}^* = 0.5$ and $\epsilon_v^* = \epsilon_I^* = \epsilon_{I_U}^* = 0.4$ and $\epsilon_v^* = \epsilon_I^* = \epsilon_{I_U}^* = 0.2$, respectively. Furthermore, the setting of $\epsilon_v^* = 0.5, \epsilon_I^* = 0.4, \epsilon_{I_U}^* = 0.3$ resulted in similar average $\epsilon_{\text{BEM}-\text{WBT}}$ error level as the setting of $\epsilon_v^* = \epsilon_I^* = \epsilon_{I_U}^* = 0.4$ (0.178 vs. 0.191) in lower total calculation times (356 minutes vs. 416 minutes). The setting of $\epsilon_v^* = 0.4, \epsilon_I^* = 0.3, \epsilon_{I_U}^* = 0.2$ also resulted in similar average $\epsilon_{\text{BEM}-\text{WBT}}$ error level as the setting of $\epsilon_v^* = \epsilon_I^* = \epsilon_{I_U}^* = 0.3$ (0.148 vs. 0.15) in lower total calculation times (426 minutes vs. 569 minutes). The same is true for the setting of $\epsilon_v^* = 0.3, \epsilon_I^* = 0.2, \epsilon_{I_U}^* = 0.1$ compared to the setting of $\epsilon_v^* = \epsilon_I^* = \epsilon_{I_U}^* = 0.2$, the average $\epsilon_{\text{BEM}-\text{WBT}}$ level being 0.113 (vs. 0.124) with a total calculation time of 779 minutes (versus 1023 minutes). It is apparent from the results of the $\epsilon_v^* = \epsilon_I^* = \epsilon_{I_U}^*$ type settings in Table 2, that at a given value of ϵ_v, the corresponding values of ϵ_I and ϵ_{I_U} are generally lower than the values of ϵ_v. Thus, the restriction of the continuity error levels (e.g., from $\epsilon_I^* = \epsilon_{I_U}^* = 0.3$ to $\epsilon_I^* = 0.2, \epsilon_{I_U}^* = 0.1$ needs less computational effort than reducing the error bound for the velocity error indicator ϵ_v (e.g., from $\epsilon_v^* = 0.3$ to $\epsilon_v^* = 0.2$). This explains the lower calculation times in the above cases. Moreover, the more restricted continuity error levels

Table 2. Results of full restart from scratch approach, threshold settings $\epsilon_v^* = \epsilon_I^* = \epsilon_{I_U}^*$. Contents of the table are the following: the solution error $\epsilon_{\mathrm{BEM-WBT}}$, total calculation time, number of DOFs in Ω_B and Ω_U, the values of the global indicators ϵ_v, ϵ_I and ϵ_{I_U}. Numerical values are provided as minimum, maximum and average values in the calculation frequency range, and as actual values at the example frequency steps of 510 Hz, 1497 Hz and 2484 Hz.

Setting	$\epsilon_{WBT-BEM}$	Time [min.]	$N_{DOF}^{\Omega_B}$	$N_{DOF}^{\Omega_U}$	ϵ_v	ϵ_I	ϵ_{I_U}
$\epsilon_v^* = 0.5$, $\epsilon_I^* = 0.5$, $\epsilon_{I_U}^* = 0.5$	0.073–0.503	310.24	2038–9294	9–729	0.191–0.487	0.117–0.378	0.062–0.496
Average:	0.246				0.365	0.214	0.211
510 Hz	0.113	0.70	2612	81	0.223	0.160	0.117
1497 Hz	0.168	2.12	4054	225	0.347	0.172	0.112
2484 Hz	0.222	7.26	7146	441	0.431	0.180	0.125
$\epsilon_v^* = 0.4$, $\epsilon_I^* = 0.4$, $\epsilon_{I_U}^* = 0.4$	0.071–0.400	416.81	2038–10740	9–1089	0.186–0.395	0.111–0.296	0.061–0.372
Average:	0.191				0.316	0.175	0.154
510 Hz	0.096	1.11	3056	81	0.212	0.143	0.110
1497 Hz	0.129	3.27	4536	225	0.313	0.152	0.103
2484 Hz	0.207	9.27	7610	441	0.368	0.166	0.121
$\epsilon_v^* = 0.3$, $\epsilon_I^* = 0.3$, $\epsilon_{I_U}^* = 0.3$	0.072–0.365	569.74	2618–11474	81–1089	0.181–0.297	0.110–0.219	0.056–0.293
Average:	0.151				0.251	0.145	0.116
510 Hz	0.091	0.88	3154	81	0.203	0.138	0.110
1497 Hz	0.116	3.72	5292	225	0.208	0.124	0.085
2484 Hz	0.190	11.29	8238	441	0.292	0.152	0.109
$\epsilon_v^* = 0.2$, $\epsilon_I^* = 0.2$, $\epsilon_{I_U}^* = 0.2$	0.065–0.278	1023.22	3158–13772	81–1089	0.150–0.200	0.077–0.189	0.037–0.192
Average:	0.124				0.182	0.121	0.090
510 Hz	0.085	1.58	3534	81	0.162	0.130	0.107
1497 Hz	0.111	3.97	5480	225	0.199	0.119	0.081
2484 Hz	0.174	22.47	9928	441	0.171	0.139	0.105
$\epsilon_v^* = 0.1$, $\epsilon_I^* = 0.1$, $\epsilon_{I_U}^* = 0.1$	0.043–0.127	N/A	6280–19726	81–2025	0.100–0.15	0.061–0.125	0.030–0.132
Average:	0.076				0.130	0.081	0.059
510 Hz	0.051	N/A	9168	225	0.104	0.076	0.048
1497 Hz	0.072	N/A	11312	441	0.110	0.071	0.031
2484 Hz	0.066	N/A	17358	729	0.137	0.069	0.046

ϵ_{I_U} on the truncation sphere do not add a significant amount of DOFs, but improve the solution accuracy in the exterior domain.

Comparing the frequency-independent *a posteriori* adaptive control (full restart from scratch approach) to the *a priori* global refinement strategies in a general sense, there are two main characteristic differences: the adaptive strategy generally yields higher number of DOFs in the low frequency range than the *a priori* strategy (with any value of T_{WF}). This also means that the adaptive strategy results in lower error levels below 500 Hz. On the other hand, in the higher frequency range, above 2500 Hz, the adaptive strategy results in lower number of DOFs, than the *a priori* strategies with the settings of $T_{WF} = 3$ and $T_{WF} = 4$. This means that the adaptive strategy results in relevant savings in the number of DOFs compared to the frequency-dependent

Table 3. Results of full restart from scratch approach, threshold settings $\epsilon_v^* = \epsilon_I^* = \epsilon_{I_U}^*$. Contents of the table are the following: the solution error $\epsilon_{\text{BEM}-\text{WBT}}$, total calculation time, number of DOFs in Ω_B and Ω_U, the values of the global indicators ϵ_v, ϵ_I and ϵ_{I_U}. Numerical values are provided as minimum, maximum and average values in the calculation frequency range, and as actual values at the example frequency steps of 510 Hz, 1497 Hz and 2484 Hz.

Setting	$\epsilon_{WBT-BEM}$	Time [min.]	$N_{DOF}^{\Omega_B}$	$N_{DOF}^{\Omega_U}$	ϵ_v	ϵ_I	ϵ_{I_U}
$\epsilon_v^* = 0.5$, $\epsilon_I^* = 0.4$, $\epsilon_{I_U}^* = 0.3$	0.072–0.369	355.98	2618–10690	81–1089	0.181–0.487	0.111–0.236	0.061–0.293
Average:	0.178				0.347	0.169	0.134
510 Hz	0.095	1.07	3142	81	0.213	0.142	0.110
1497 Hz	0.133	2.90	4644	225	0.329	0.151	0.102
2484 Hz	0.222	6.78	7242	441	0.432	0.179	0.126
$\epsilon_v^* = 0.4$, $\epsilon_I^* = 0.3$, $\epsilon_{I_U}^* = 0.2$	0.069–0.274	426.69	2924–11258	81–1089	0.180–0.396	0.111–0.203	0.061–0.195
Average:	0.148				0.306	0.149	0.112
510 Hz	0.090	0.84	3228	81	0.203	0.138	0.110
1497 Hz	0.124	2.17	4734	225	0.310	0.146	0.102
2484 Hz	0.207	8.78	7610	441	0.368	0.166	0.121
$\epsilon_v^* = 0.3$, $\epsilon_I^* = 0.2$, $\epsilon_{I_U}^* = 0.1$	0.066–0.183	779.55	3216–14202	81–1521	0.161–0.300	0.090–0.176	0.050–0.098
Average:	0.113				0.240	0.121	0.078
510 Hz	0.082	1.73	3872	225	0.177	0.115	0.084
1497 Hz	0.105	4.29	5548	441	0.199	0.114	0.064
2484 Hz	0.144	13.50	8998	729	0.279	0.128	0.059

global refinement. While this already relaxes the memory requirements to store the fully populated system matrix, the time cost of the adaptive strategy is not only dependent on the number of the DOFs, but also on the effort spent on the iterative recalculations to achieve the prescribed indicator levels. Comparing the time cost vs. accuracy, the error level of the setting $T_{WF} = 3$ (reference for comparison) is similar to the error level of the settings $\epsilon_v^* = 0.2, \epsilon_I^* = 0.2, \epsilon_{I_U}^* = 0.2$ and $\epsilon_v^* = 0.3, \epsilon_I^* = 0.2, \epsilon_{I_U}^* = 0.1$. The time costs of the setting $\epsilon_v^* = 0.3, \epsilon_I^* = 0.2, \epsilon_{I_U}^* = 0.1$ and the *a priori* setting of $T_{WF} = 3$ is similar (779 minutes vs. 768 minutes). Furthermore, both settings of the adaptive strategy are relevantly faster than the *a priori* setting of $T_{WF} = 4$, which however yields lower error levels above 1500 Hz, than the adaptive results. The adaptive strategy with threshold levels in the range of 0.4–0.5 are significantly faster than the global refinement with the truncation factor of $T_{WF} = 2$, while the adaptive calculation provides more controlled error levels.

It is apparent from all the above, that the adaptive strategy results in lower error levels in the low-frequency range, at a cost of higher number of DOFs and thus higher calculation times. On the other hand it results in relevant savings in DOFs in the higher frequency region. Still, the total calculation time of the recalculate from scratch approach is higher, which is caused by the time overhead spent on the unsuccessful recalculations/iterations to achieve the prescribed error indicator thresholds.

6.2.6. Combined strategy

To reduce the time overhead of the full "recalculate from scratch" to some extent, it is beneficial to use the combined adaptive local refinement presented in Subsec. 4.2.2, which utilizes an *a priori*, frequency-dependent initial wave function configuration. The selection of an appropriate, low trun-

cation factor is crucial to avoid a homogeneous over-refinement already in the initial step. For the initial wave function configuration, the truncation values of $T^0_{WF} = 2$ and $T^0_{RF} = 0.5$ were chosen. According to (19), the initial wave function set is further refined iteratively using local refinement based on the error indicators. Further parameters of the combined control rule (19) were the following: the increase step of $M^{(\alpha)}$ was 1 and the increase step for N was 6 (identically to the full restart from scratch).

Table 4 presents the results of the combined strategy in the range of 0.1–0.3 boundary error threshold levels. Since the initial parameters of the wave function sets are frequency dependent, and the increase step parameters are the same as for "recalculate from scratch approach", the combined strategy results in somewhat different wave function set configurations (and number of DOFs). The error and indicator levels are not significantly different. Compared to the full restart from scratch approach, the calculation times are reduced by 5–32% percent depending on the threshold settings. Consequently, the combined control with the threshold setting of $\epsilon^*_v = 0.3, \epsilon^*_I = 0.2, \epsilon^*_{I_U} = 0.1$ became faster than the (reference) *a priori* setting of $T_{WF} = 3$, while achieving similar accuracy. The setting of $\epsilon^*_v = 0.2, \epsilon^*_I = 0.2, \epsilon^*_{I_U} = 0.2$ became faster by approximately 22% than the same setting using the full "recalculate from scratch approach". Moreover, both settings of the combined strategy are faster by approximately two times, than the *a priori* setting of $T_{WF} = 4$.

Table 4. Results of the combined *a priori/a posteriori* control strategy. Contents of the table are the following: the solution error $\epsilon_{\mathrm{BEM-WBT}}$, total calculation time, number of DOFs in Ω_B and Ω_U., the values of the global indicators ϵ_v, ϵ_I and ϵ_{I_U}. Numerical values are provided as minimum, maximum and average values in the calculation frequency range, and as actual values at the example frequency steps of 510 Hz, 1497 Hz and 2484 Hz.

Setting	$\epsilon_{WBT-BEM}$	Time [min.]	$N^{\Omega_B}_{DOF}$	$N^{\Omega_U}_{DOF}$	ϵ_v	ϵ_I	ϵ_{I_U}
$\epsilon^*_v = 0.3$, $\epsilon^*_I = 0.3$, $\epsilon^*_{I_U} = 0.3$	0.098–0.246	387.31	1774–10320	36–1296	0.207–0.299	0.120–0.231	0.057–0.280
Average:	0.155				0.262	0.168	0.113
510 Hz	0.167	0.43	1838	36	0.299	0.231	0.232
1497 Hz	0.152	1.58	3706	144	0.291	0.166	0.112
2484 Hz	0.202	11.82	8124	676	0.248	0.168	0.118
$\epsilon^*_v = 0.3$, $\epsilon^*_I = 0.2$, $\epsilon^*_{I_U} = 0.1$	0.046–0.184	743.77	2250–12216	196–2401	0.117–0.298	0.091–0.154	0.048–0.100
Average:	0.118				0.244	0.125	0.071
510 Hz	0.094	2.67	3220	576	0.188	0.127	0.087
1497 Hz	0.113	2.44	4590	484	0.293	0.137	0.082
2484 Hz	0.150	11.35	8922	1024	0.296	0.124	0.067
$\epsilon^*_v = 0.2$, $\epsilon^*_I = 0.2$, $\epsilon^*_{I_U} = 0.2$	0.067–0.252	806.44	2594–12692	49–1600	0.146–0.196	0.084–0.176	0.042–0.179
Average:	0.118				0.182	0.122	0.079
510 Hz	0.118	1.34	2766	144	0.160	0.157	0.108
1497 Hz	0.099	5.40	5849	370	0.188	0.105	0.063
2484 Hz	0.122	20.79	10756	676	0.168	0.105	0.054
$\epsilon^*_v = 0.1$, $\epsilon^*_I = 0.1$, $\epsilon^*_{I_U} = 0.1$	0.040–0.130	N/A	5740–20236	121–3600	0.100–0.16	0.061–0.118	0.027–0.167
Average:	0.076				0.128	0.080	0.053
510 Hz	0.051	N/A	8180	324	0.103	0.074	0.046
1497 Hz	0.060	N/A	12330	784	0.106	0.067	0.048
2484 Hz	0.083	N/A	14386	1024	0.142	0.102	0.068

Figure 6 depicts the results obtained by the combined strategy with the settings of $\epsilon_v^* = \epsilon_I^* = \epsilon_{I_U}^* = 0.4$ and $\epsilon_v^* = \epsilon_I^* = \epsilon_{I_U}^* = 0.2$ along with results of the *a priori* global refinement. The characteristic differences between the adaptive solution and the *a priori* strategy mentioned in Subsec. 6.2.5 are evident from this figure. The combined adaptive strategy with the setting of $\epsilon_v^* = \epsilon_I^* = \epsilon_{I_U}^* = 0.2$ results in higher number of DOFs in the low frequency region below 500 Hz than the *a priori* global refinement, where the *a priori* refinement typically yields higher error levels. Above 2000 Hz, the adaptive strategy spares the number of DOFs compared to the *a priori* setting of $T_{WF} = 3$. In the most time-critical frequency region, above 2500 Hz, where the *a priori* global refinement results in excessive calculation times, the threshold setting of $\epsilon_v^* = \epsilon_I^* = \epsilon_{I_U}^* = 0.2$ yields lower calculation times. The $\epsilon_{\text{BEM}-\text{WBT}}$ error level of both the settings of $\epsilon_v^* = \epsilon_I^* = \epsilon_{I_U}^* = 0.2$ and $\epsilon_v^* = \epsilon_I^* = \epsilon_{I_U}^* = 0.4$ show a more controlled behavior, than it is in the case of the *a priori* refinement.

6.2.7. Pressure field results

Figure 7 shows pressure field results obtained by the combined adaptive calculation strategy with the settings of $\epsilon_v^* = 0.2, \epsilon_I^* = 0.2, \epsilon_{I_U}^* = 0.2$ along with the reference pressure results of BEM. For the

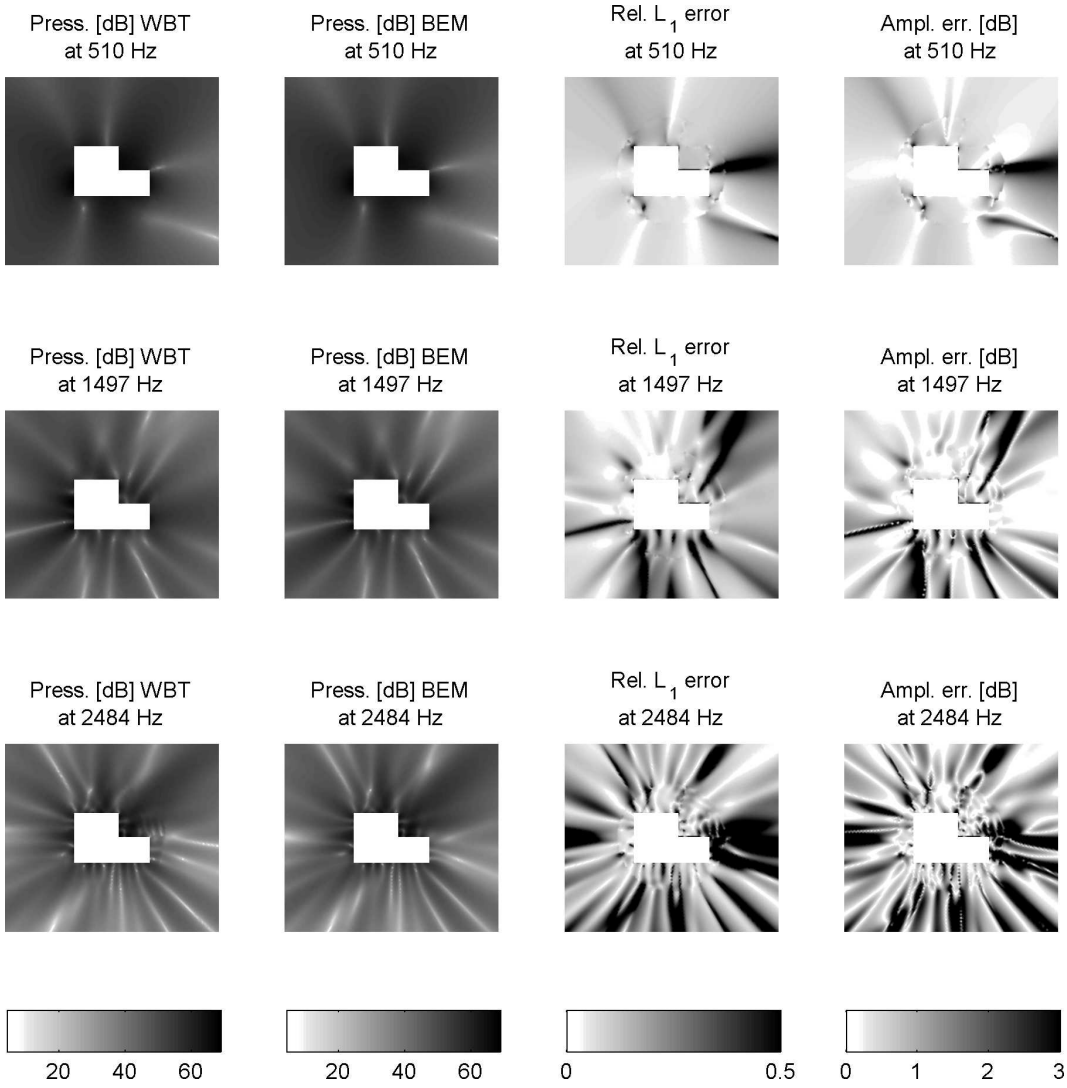

Fig. 7. Pressure [dB_{SPL}] plots of the engine model along with the pointwise relative L_1 pressure error and amplitude error distribution depicted at 510 Hz, 1497 Hz and 2484 Hz.

sake of the visual assessment of the approximation error, the pointwise relative L_1-norm pressure error distribution and the amplitude error are also plotted. The selected field-point plane cuts through the main axis of the engine. The pointwise L_1-norm pressure error is defined in the i-th field point as $|p_{i_{\mathrm{BEM}}} - p_{i_{\mathrm{WBT}}}|/|p_{i_{\mathrm{BEM}}}|$, while the amplitude error in dB is defined as $|p_{i_{\mathrm{BEM}}}[dB] - p_{i_{\mathrm{WBT}}}[\mathrm{dB}]|$. It is evident that a very good agreement with the reference result of BEM was obtained, and an excellent absolute error level of approximately 1-2 dB was achieved in the whole frequency range. The relative L_1 error and the amplitude error show higher values in the low-pressure areas, where the error calculation itself is also unstable due to small numeric reference values.

7. Conclusions

This paper presented an industrial-oriented application of a novel, adaptive wave-based technique based on boundary error indicators for the sound radiation simulation of a combustion engine. The introduced error indicators were defined in the relative L_2 norm, and they evaluate the deviation of the numerical solution from the prescribed boundary conditions and the coupling mismatch on the coupling interfaces between adjacent subdomains. The proposed relative L_2-norm error indicators control an adaptive local refinement strategy, which refines and iteratively recalculates the numerical solution of WBT. Two different approaches were adopted and presented for the adaptive control strategy: a frequency-independent *a posteriori* wave function control, which implements an iterative full "restart from scratch approach" at each frequency step and a combined *a priori/a posteriori* approach, in which the initial wave function configuration is dependent on the calculation frequency.

Accuracy of the results has been compared with reference quality BE results. The reference BE model in the present work is based on a relatively fine mesh, and is aimed to provide reference quality results. Therefore, presented calculation times of the academic MATLAB implementation of WBT are not meant to be compared to the calculation times of the BE reference model. Therefore, a thorough efficiency evaluation and comparison to BEM was not a goal of the present paper.

The main focus of the investigation was to provide results with an engineering accuracy of approx. 10% and to assess the potentials of the adaptive strategy at this accuracy level. Therefore, a brief parametric analysis of the error thresholds was presented in the range of 0.1–0.5 error indicator thresholds. The efficiency of the adaptive solution schemes was compared to the results of *a priori*, frequency-independent global refinement strategies.

It was found that the adaptive strategy generally yields higher number of DOFs and, as a result, longer calculation times in the low frequency range than the *a priori* global refinement. It also provides lower error levels in the low frequency range. In the higher frequency region of the calculations, the frequency-dependent global refinement excessively increases the number of DOFs and the calculation time, which results in decreasing error levels with increasing frequency, if the global truncation parameter was high enough.

The adaptive calculations resulted in lower number of DOFs than the *a priori* calculations in the higher frequency region of the calculations, and this already reduces the memory requirements of the method. On the other hand, the assessment in terms of calculation time revealed that full recalculate from scratch approach resulted in longer calculation times in the accuracy range of 10% than the *a priori* global refinement with the same accuracy.

The combined *a priori/a posteriori* wave function control strategy resulted in reduced calculation times compared to the full "restart from scratch approach". It was established that the combined strategy results in similar or shorter calculation times and reduced memory consumption in comparison to the global refinement, while providing more controlled error levels.

The presented adaptive calculation strategy based on the proposed boundary error indicators provides an interesting and efficient alternative to implement a p-refinement scheme for the WBT. Although the presented error control strategy provides no rigorous error estimation, it is a valuable tool to control and monitor the accuracy of the calculation in the practical application of the wave-based technique.

8. Acknowledgements

This work was partially funded by the scholarship of the Marie Curie Host Fellowship for Early Stage Research Training (EST) within the SIMVIA2 project (MEST-CT-2005-020263) of the Sixth Framework Programme (FP6) of the European Union. Furthermore, the work was also funded by the financial support of the COMET K2 Competence Centers for Excellent Technologies Programme of the Austrian Federal Ministry for Transport, Innovation and Technology (BMVIT), the Austrian Federal Ministry of Economy, Family and Youth (BMWFJ), the Austrian Research Promotion Agency (FFG), and the Province of Styria and the Styrian Business Promotion Agency (SFG).

References

[1] O.C. Zienkiewicz. *The finite element method*. McGraw-Hill, London, New York, 3rd expanded and revised edition, 1977.

[2] F. Ihlenburg. *Finite element analysis of acoustic scattering*. Springer, Berlin, 1998.

[3] S. Kirkup. *The boundary element method (BEM) in acoustics*. Integrated Sound Software, 1998.

[4] T.W. Wu. *Boundary element acoustics: fundamentals and computer codes*. WIT Press, 2000.

[5] I. Harari, T.J.R. Hughes. Finite element methods for the Helmholtz equation in an exterior domain: model problems. *Computer Methods in Applied Mechanics and Engineering*, **87**(1): 59–96, 1991.

[6] F. Ihlenburg, I. Babuska. Finite element solution of the Helmholtz equation with high wave number, part I: the h-version of the FEM. *Computers and Mathematics with Applications*, **30**(9): 9–37, 1995.

[7] I.G. Graham, M. Löhndorf, J.M. Melenk, E.A. Spence. When is the error in the h-BEM for solving the Helmholtz equation bounded independently of k?. *BIT Numerical Mathematics*, **55**(1): 171–214, 2015.

[8] S. Marburg, B. Nolte. *Computational acoustics of noise propagation in fluids – finite and boundary element methods*. Springer-Verlag, Berlin, Heidelberg, 2008.

[9] I.M. Babuska, S.A. Sauter. Is the pollution effect of the FEM avoidable for the Helmholtz equation considering high wave numbers? *SIAM Review*, **42**(3): 451–484, 2000.

[10] F. Ihlenburg. The medium-frequency range in computational acoustics: practical and numerical aspects. *Journal of Computational Acoustics*, **11**(2): 175–193, 2003.

[11] J.T. Oden, S. Prudhomme, L. Demkowicz. A posteriori error estimation for acoustic wave propagation problems. *Archives of Computational Methods in Engineering*, **12**(4): 343–389, 2005.

[12] M. Ainsworth, J.T. Oden. *A posteriori error estimation in finite element analysis*. Pure and Applied Mathematics Series. John Wiley, 2000.

[13] J.R. Stewart, T.J.R. Hughes. An a posteriori error estimator and hp-adaptive strategy for finite element discretizations of the Helmholtz equation in exterior domains. *Finite Elements in Analysis and Design, Adaptive Meshing, Part 1*, **25**(1–2): 1–26, 1997.

[14] J.R. Stewart, T.J.R. Hughes. A posteriori error estimation and adaptive finite element computation of the Helmholtz equation in exterior domains. *Finite Elements in Analysis and Design, Special Issue: Robert J. Melosh Medal Competition*, **22**(1): 15–24, 1996.

[15] J.R. Stewart, T.J.R. Hughes. Explicit residual-based a posteriori error estimation for finite element discretizations of the Helmholtz equation: computation of the constant and new measures of error estimator quality. *Computer Methods in Applied Mechanics and Engineering*, **131**(3–4): 335–363, 1996.

[16] S. Irimie, Ph. Bouillard. A residual a posteriori error estimator for the finite element solution of the Helmholtz equation. *Computer Methods in Applied Mechanics and Engineering*, **190**(31): 4027–4042, 2001.

[17] F. Ihlenburg, T. Strouboulis, S.K. Gangaraj, I. Babuska. A posteriori error estimation for finite element solutions of Helmholtz' equation, part I: the quality of local indicators and estimators. *International Journal for Numerical Methods in Engineering*, **40**(18): 3443–3462, 1997.

[18] T. Strouboulis, I. Babuska, S.K. Gangaraj. Guaranteed computable bounds for the exact error in the finite element solution, part I: one-dimensional model problem. *Computer Methods in Applied Mechanics and Engineering*, **176**(1–4): 51–79, 1999.

[19] T. Strouboulis, I. Babuska, S.K. Gangaraj. Guaranteed computable bounds for the exact error in the finite element solution, part II: bounds for the energy norm of the error in two dimensions. *International Journal for Numerical Methods in Engineering*, **47**(1–3): 427–475, 2000.

[20] F. Ihlenburg, Ph. Bouillard. Error estimation and adaptivity for the finite element method in acoustics: 2D and 3D applications. *Computer Methods in Applied Mechanics and Engineering*, **176**(1–4): 147–163, 1999.

[21] F. Ihlenburg, T. Strouboulis, S.K. Gangaraj, I. Babuska. A posteriori error estimation for finite element solutions of Helmholtz equation – part II: estimation of the pollution error. *International Journal for Numerical Methods in Engineering*, **40**(21): 3883–3900, 1997.

[22] S. Prudhomme, J.T. Oden. On goal-oriented error estimation for elliptic problems: application to the control of pointwise errors. *Computer Methods in Applied Mechanics and Engineering*, **176**(1–4): 313–331, 1999.

[23] J. Sarrate, J. Peraire, A. Patera. A posteriori finite element error bounds for non-linear outputs of the Helmholtz equation. *International Journal for Numerical Methods in Fluids*, **31**(1): 17–36, 1999.

[24] L. Banjai, S. Sauter. A refined Galerkin error and stability analysis for highly indefinite variational problems. *SIAM J. Numer. Anal.*, **45**(1): 37–53, January 2007.

[25] A. Karafiat. Adaptive boundary element method for acoustic scattering problems. *Journal of Theoretical and Applied Mechanics*, **36**(2), 423–436, 1998.

[26] L. Demkowicz, J.T. Oden. Recent progress on application of *hp*-adaptive BE/FE methods to elastic scattering. *International Journal for Numerical Methods in Engineering*, **37**(17): 2893–2910, 1994.

[27] E. Kita, N. Kamiya. Error estimation and adaptive mesh refinement in boundary element method. an overview. *Engineering Analysis with Boundary Elements*, **25**(7): 479–495, 2001.

[28] J.M. Melenk, I. Babuška. *The partition of unity finite element method: basic theory and applications*. TICAM report. Texas Institute for Computational and Applied Mathematics, University of Texas at Austin, 1996.

[29] P. Massimi, R. Tezaur, Ch. Farhat. A discontinuous enrichment method for three-dimensional multiscale harmonic wave propagation problems in multi-fluid and fluid-solid media. *International Journal for Numerical Methods in Engineering*, **76**(3): 400–425, 2008.

[30] I. Harari. A survey of finite element methods for time-harmonic acoustics. *Computer Methods in Applied Mechanics and Engineering, A Tribute to Thomas J.R. Hughes on the Occasion of his 60th Birthday,* **195**(13–16): 1594–1607, 2006.

[31] M. Fischer, U. Gauger, L. Gaul. A multipole Galerkin boundary element method for acoustics. *Engineering Analysis with Boundary Elements*, **28**(2): 155–162, 2004.

[32] D.W. Herrin, F. Martinus, T.W. Wu, A.F. Seybert. An assessment of the high frequency boundary element and Rayleigh integral approximations. *Applied Acoustics*, **67**(8): 819–833, 2006.

[33] N.A Gumerov, R. Duraiswami. *Fast multipole methods for the Helmholtz equation in three dimensions*. Elsevier Science, 2005.

[34] E. Trefftz. Ein Gegenstück zum ritzschen Verfahren, A counterpart to Ritz's method. *Proceedings of the 2nd International Congress on Applied Mechanics*, pp. 131–137, 1926.

[35] E. Kita, N. Kamiya. Trefftz method: an overview. *Advances in Engineering Software*, **24**(1–3): 3–12, 1995.

[36] B. Pluymers, B. van Hal, D. Vandepitte, W. Desmet. Trefftz-based methods for time-harmonic acoustics. *Archives of Computational Methods in Engineering*, **14**: 343–381, 2007.

[37] E. Deckers, O. Atak, L. Coox, R. D'Amico, H. Devriendt, S. Jonckheere, K. Koo, B. Pluymers, D. Vandepitte, W. Desmet. The wave based method: an overview of 15 years of research. *Wave Motion*, **51**(4): 550–565, 2014.

[38] W. Desmet. *A wave based prediction technique for coupled vibro-acoustic analysis*. PhD thesis, Katholieke Universiteit Leuven, Leuven, 1998.

[39] C. Vanmaele, D. Vandepitte, W. Desmet. An efficient wave based prediction technique for plate bending vibrations. *Computer Methods in Applied Mechanics and Engineering*, **196**(33–34): 3178–3189, 2007.

[40] C. Vanmaele, D. Vandepitte, W. Desmet. An efficient wave based prediction technique for dynamic plate bending problems with corner stress singularities. *Computer Methods in Applied Mechanics and Engineering*, **198**(30–32): 2227–2245, 2009.

[41] B. Pluymers, W. Desmet, D. Vandepitte, P. Sas. Application of an efficient wave-based prediction technique for the analysis of vibro-acoustic radiation problems. *Journal of Computational and Applied Mathematics, Selected Papers from the Second International Conference on Advanced Computational Methods in Engineering (ACOMEN 2002)*, 168(1–2): 353–364, 2004.

[42] B. Van Genechten, K. Vergote, D. Vandepitte, W. Desmet. A multi-level wave based numerical modelling framework for the steady-state dynamic analysis of bounded Helmholtz problems with multiple inclusions. *Computer Methods in Applied Mechanics and Engineering*, **199**(29–32): 1881–1905, 2010.

[43] B. Van Genechten, B. Bergen, D. Vandepitte, W. Desmet. A Trefftz-based numerical modelling framework for Helmholtz problems with complex multiple-scatterer configurations. *Journal of Computational Physics*, **229**(18): 6623–6643, 2010.

[44] W. Desmet, B. van Hal, P. Sas, D. Vandepitte. A computationally efficient prediction technique for the steady-state dynamic analysis of coupled vibro-acoustic systems. *Advances in Engineering Software*, **33**(7–10): 527–540, 2002.

[45] B. van Hal, W. Desmet, D. Vandepitte, P. Sas. *Coupled finite element-wave-based approach in steady-state structural acoustics*. Computational Fluid and Solid Mechanics 2003, K.J. Bathe [Ed.], pp. 1552–1555, Elsevier Science Ltd, Oxford, 2003.

[46] B. van Hal, W. Desmet, D. Vandepitte. Hybrid finite element – wave-based method for steady-state interior structural-acoustic problems. *Computers and Structures, Advances in Analysis of Fluid Structure Interaction*, **83**(2–3): 167–180, 2005.

[47] B. Pluymers, A. Hepberger, W. Desmet, H.H. Prebsch, D. Vandepitte, P. Sas. *Experimental validation of the wave-based prediction technique for the analysis of the coupled vibro-acoustic behavior of a 3D cavity*. Computational Fluid and Solid Mechanics 2003, K.J. Bathe [Ed.], pp. 1483–1487, Elsevier Science Ltd, Oxford, 2003.

[48] B. Van Genechten, D. Vandepitte, W. Desmet. A direct hybrid finite element – wave-based modelling technique for efficient coupled vibro-acoustic analysis. *Computer Methods in Applied Mechanics and Engineering*, **200**(5–8): 742–764, 2011.

[49] F. Diwoky, A. Hepberger, T. Mocsai, H. Pramberger, H.-H. Priebsch. Application of the wave based technique to 3D radiation problems. *Proc. of the LSAME 2008 Trefftz Symposium, Leuven, Belgium*, 2008.

[50] T. Mocsai, A. Hepberger, F. Diwoky, H.-H. Priebsch. Investigations on potential improvements of the wave based technique for the application to radiation problems under anechoic conditions. *Proc. of ISMA 2008 – International Conference on Noise and Vibration Engineering, Leuven, Belgium*, 2008.

[51] T. Mocsai, A. Hepberger, F. Diwoky, H.-H. Priebsch. Engine radiation simulation up to 3 kHz using the wave based technique. *Proc. of the ICSV 2009 – The 16th International Congress on Sound and Vibration, Krakow, Poland*, 2009.

[52] T. Mocsai, F. Diwoky, H.-H. Priebsch. The application of the wave based technique for 3D free-field radiation calculation using a residual error controlled adaptive strategy. In *Proc. of ISMA 2010 – International Conference on Noise and Vibration Engineering, Leuven, Belgium*, 2010.

[53] F. Augusztinovicz, T. Mócsai. Application and analysis of a boundary error indicator based adaptive wave based technique. *AIA-DAGA 2013 Conference on Acoustics*, 2013.

[54] J. Jegorovs. On the convergence of the WBM solution in certain non-convex domains. *Proc. of the International Conference on Noise and Vibration Engineering ISMA 2006*, 2006.

[55] B. Pluymers. *Wave based modelling methods for steady-state vibro-acoustics*. PhD thesis, Katholieke Universiteit Leuven, Leuven, 2006.

[56] R. Courant, D. Hilbert. *Methods of mathematical physics, Vol. 1*. Wiley, 2008.

[57] P. Gamallo, R.J. Astley. A comparison of two Trefftz-type methods: the ultraweak variational formulation and the least-squares method, for solving shortwave 2-D Helmholtz problems. *International Journal for Numerical Methods in Engineering*, **71**(4): 406–432, 2007.

[58] M.H. Protter, H.F. Weinberger. *Maximum principles in differential equations*. Englewood Cliffs, N.J., Prentice-Hall, 1967.

[59] R. Schaback. A posteriori error bounds for meshless methods. *Proc. of ECCOMAS 2007 (European Congress on Computational Methods in Applied Sciences and Engineering)*, 2007.

[60] V.G. Sigillito. *Explicit a priori inequalities with applications to boundary value problems*. Pitman Publishing, 1977.

[61] G. Still. Computable bounds for eigenvalues and eigenfunctions of elliptic differential operators. *Numerische Mathematik*, **54**: 201–223, 1989.

[62] J.R. Kuttler, V.G. Sigillito. Bounding eigenvalues of elliptic operators. *SIAM Journal on Mathematical Analysis*, **9**(4): 768–773, 1978.

[63] A.H. Barnett, T. Betcke. Stability and convergence of the method of fundamental solutions for Helmholtz problems on analytic domains. *Journal of Computational Physics*, **227**(14): 7003–7026, 2008.

[64] A.H. Barnett. Perturbative analysis of the method of particular solutions for improved inclusion of high-lying Dirichlet eigenvalues. *SIAM Journal on Numerical Analysis*, **47**(3): 1952–1970, 2009.

[65] A.H. Barnett, A. Hassell. Boundary quasi-orthogonality and sharp inclusion bounds for large Dirichlet eigenvalues, 2010. arXiv:1006.3592 [math.AP]

[66] Z.C. Lu. *Trefftz and collocation methods*. WIT Press, 2008.

[67] Z.C. Li. The Trefftz method for the Helmholtz equation with degeneracy. *Applied Numerical Mathematics*, **58**: 131–159, February 2008.

[68] J.B. Fahnline. *The generalized inverse source method for the computation of acoustic fields*. PhD thesis, Pennsylvania State University, 1993.

[69] G.H. Koopmann, L. Song, J.B. Fahnline. A method for computing acoustic fields based on the principle of wave superposition. *J. Acoust. Soc. Am.*, **86**(6): 2433–2438, 1989.

[70] L. Song, G.H. Koopmann, J.B. Fahnline. Numerical errors associated with the method of superposition for computing acoustic fields. *J. Acoust. Soc. Am.*, **89**(6): 2625–2633, 1991.

[71] J.A. Kolodziej, R. Starosta. Self-adaptive Trefftz procedure for harmonic problems. *First International Workshop on the Trefftz Method, Computer Assisted Mechanics and Engineering Sciences*, **4**: 491–500, 1997.

[72] B. Van Hal. *Automation and performance optimization of the wave based method for interior structural-acoustic problems*. PhD thesis, Katholieke Universiteit Leuven, Leuven, 2004.

[73] L.F. Shampine. Vectorized adaptive quadrature in MATLAB. *Journal of Computational and Applied Mathematics*, **211**(2): 131–140, 2008.

[74] G. Offner. Modelling of condensed flexible bodies considering non-linear inertia effects resulting from gross motions. *Journal of Multi-body Dynamics. Proceedings of the Institution of Mechanical Engineers, Part K*, 2009.

[75] H.H. Priebsch, G. Offner, H.M. Herbst. A generic simulation model for cylinder kit vibro-acoustics, part II: piston slap and engine structure interaction. *Proceedings of ASME ICE Spring Technical Conference*, 2003.

[76] B. Loibnegger, H.H. Priebsch, I. McLuckie, M.T. Ma, G. Offner. A fast approach to model hydrodynamic behaviour of journal bearings for analysis of crankshaft and engine dynamics. *30th Leeds-Lyon Symposium on Tribology*, 2003.

[77] D. Colton, R. Kress. *Inverse acoustic and electromagnetic scattering theory (applied mathematical sciences)*. Springer, 2nd edition, January 1998.

[78] R. Coifman, V. Rokhlin, S. Wandzura. The fast multipole method for the wave equation: a pedestrian prescription. *IEEE Antennas and Propagation Magazine*, **35**(3): 7–12, 1993.

[79] E. Darve. The fast multipole method, part I: error analysis and asymptotic complexity. *SIAM Journal on Numerical Analysis*, **38**(1): 98–128, 2001.